

On the dynamics of persistent states and their secular trends in the waveguides of the Southern Hemisphere troposphere

Terence J. O’Kane¹ · James S. Risbey¹ · Didier P. Monselesan¹ · Illia Horenko² · Christian L. E. Franzke³

Received: 7 May 2015 / Accepted: 26 July 2015
© Springer-Verlag Berlin Heidelberg 2015

Abstract We identify the dynamical drivers of systematic changes in persistent quasi-stationary states (regimes) of the Southern Hemisphere troposphere and their secular trends. We apply a purely data-driven approach, whereby a multiscale approximation to nonstationary dynamical processes is achieved through optimal sequences of locally stationary fast vector autoregressive factor processes, to examine a high resolution atmospheric reanalysis over the period encompassing 1958–2013. This approach identifies regimes and their secular trends in terms of the predictability of the flow and is Granger causal. A comprehensive set of diagnostics on both isentropic and isobaric surfaces is employed to examine teleconnections over the full hemisphere and for a set of regional domains. Composite states for the hemisphere obtained from nonstationary nonparametric cluster analysis reveal patterns consistent with a circumglobal wave 3 (polar)–wave 5 (subtropical) pattern, while regional composites reveal the Pacific South

American pattern and blocking modes. The respective roles of potential vorticity sources, stationary Rossby waves and baroclinic instability on the dynamics of these circulation modes are shown to be reflected by the seasonal variations of the waveguides, where Rossby wave sources and baroclinic disturbances are largely contained within the waveguides and with little direct evidence of sustained remote tropical influences on persistent synoptic features. Warm surface temperature anomalies are strongly connected with regions of upper level divergence and anticyclonic Rossby wave sources. The persistent states identified reveal significant variability on interannual to decadal time scales with large secular trends identified in all sectors apart from a region close to South America.

Keywords Atmospheric teleconnections · Baroclinic instability · Rossby waves · Waveguides · Regimes · Secular trends

✉ Terence J. O’Kane
terence.okane@csiro.au

James S. Risbey
james.risbey@csiro.au

Didier P. Monselesan
didier.monselesan@csiro.au

Illia Horenko
illia.horenko@usi.ch

Christian L. E. Franzke
christian.franzke@uni-hamburg.de

- ¹ CSIRO Oceans and Atmosphere, Hobart, Australia
- ² Universita della Svizzera, Italiana, Lugano, Switzerland
- ³ Meteorological Institute and Center for Earth System Research and Sustainability, University of Hamburg, Hamburg, Germany

1 Introduction

The importance of the formation (onset) and decay of persistent coherent features to understanding the predictability of the midlatitude synoptic atmospheric circulation has been recognised since the earliest days of numerical weather prediction (Charney 1947; Eady 1949; Phillips 1954). Such features are described in meteorology as teleconnection patterns and are often associated with regional patterns of the leading eigenvectors obtained via singular value decomposition (Barnston and Livezey 1987). Eigenvector methods, such as empirical orthogonal functions (EOFs) (Lorenz 1956; Hannachi et al. 2007), generally assume that the timeseries in question is statistically stationary, decomposing the data according to modes that

maximise the variance. From conceptual and mathematical viewpoints, such methods do not account for the relative persistence of spatially coherent structures and are entirely framed in terms of the stationary (i.e., time-independent) covariances (correlation). Nevertheless, eigenvector methods can give robust results for some of the leading modes of the midlatitude tropospheric circulation, but higher order modes that explain progressively less variance are harder to interpret (see Risbey et al. (2015) for a more complete discussion). Accurate characterisation of atmospheric blocking in the Southern Hemisphere (SH) for example requires at least the leading nine EOFs (O’Kane et al. 2013). In the application of dynamical systems theory to the midlatitude atmospheric circulation (Legras and Ghil 1985), quasi-stationary structures are most commonly referred to as regimes and or persistent or metastable states. The existence of multiple equilibria in terms of blocked or zonal states in the troposphere was first proposed by Charney and DeVore (1979) (see also the more recent re-examinations of Lorenz 2006; Zidikheri et al. 2007).

It is generally accepted that the circulation is not statistically stationary and both secular trends in persistence as well as evolving structural changes to atmospheric teleconnections in response to combined natural variability and external forcings such as anthropogenic CO₂ may be present (Freitas et al. 2015; Franzke et al. 2015). Ideally, one would like to formulate nonstationary timeseries analysis methods in terms of the predictability of the flow and not infer causal relationships from correlations (Granger 1988; Gerber and Horenko 2014). To this end, the finite element, bounded variation, non-parametric vector autoregressive factor method (FEM-BV-VARX) has been developed for general non-stationary time series (Horenko 2010a, b, 2011; Metzner et al. 2012). Using a general variational framework including regularisation, the approach is to fit vector autoregressive models to the data to simultaneously estimate metastable states and the most probable transitions between them (Akaike 1974; Burnham and Anderson 2002). Information Theory is employed to determine the optimal set of model parameters and account for parsimony. The method is general and can be applied to Bernoulli, Markov and non-Markovian processes, where unresolved scales are parameterised as a stochastic process. Importantly, it makes no a priori probabilistic assumptions about the structure of the data, except that the flow switches between a finite number of persistent states or regimes i.e. the method is non-parametric. Here we apply the FEM-BV-VARX methodology making comparison to teleconnections determined by EOF/PCA where appropriate.

The generation and propagation of Rossby waves is integral to describing how coherent structures form in the atmosphere on synoptic timescales. There are two prevailing paradigms for understanding the propagation of these

waves and their role in the formation of quasi-stationary structures in observed atmospheric patterns. The first arose from linear wave theory in a barotropic atmosphere i.e. Rossby wave propagation through a horizontally varying medium (Hoskins and Karoly 1981; Branstator 1983; Hoskins and Ambrizzi 1993). In particular Hoskins and Karoly (1981) and later Karoly (1983) applied ray tracing to consider the propagation of stationary planetary waves in a zonally symmetric barotropic atmosphere. These studies, based on linear-steady state assumptions, show the crucial role of subtropical forcing in the westerly wind region to middle latitude dynamics, and that stationary waves appear in response to slowly time varying forcing. Using a baroclinic model with anomalous tropical heating, Qin and Robinson (1993) determined that for the extratropics there exists a balance between vortex stretching and vorticity advection by the nondivergent flow, largely due to geostrophy, and that baroclinic features are essential for the organisation of coherent Rossby wave sources. Later it was determined that the subtropical and polar jet streams act as wave guides for the main stationary Rossby wave activity (Hoskins and Ambrizzi 1993; Ambrizzi et al. 1995; Ambrizzi and Hoskins 1997). More recently Li et al. (2015) used the ray tracing method to examine the role of stationary Rossby waves generated by tropical Atlantic sea surface temperature changes and circulation anomalies around Antarctica during austral winter. In this paradigm Rossby wave propagation is considered in the stationary case where it is assumed that the background flow is stable to small perturbations—therefore requiring a source, usually in the form of anomalously large and persistent thermal or sea surface temperatures (SST), for Rossby wave generation.

The second paradigm proposed by Frederiksen (Frederiksen 1982, 1983; Frederiksen and Webster 1988) and supported by the observational studies of Dole (Dole and Gordon 1983; Dole 1986) and those of Colucci (Colucci 1985, 1987), assumes that the background flow is unstable to small perturbations and that coherent features may form where instabilities grow and become resonant with Rossby waves. Where Rossby waves interact strongly with topography (topographic trapping), such resonant interactions are more likely to occur and the flow transitions from zonal to blocked are more probable. In this paradigm, growing baroclinic instabilities are largely responsible for the onset of the coherent structure. Both paradigms support the idea that barotropic instability, often in the form of potential vorticity generation due to Rossby waves breaking on the mature coherent structure (Luo et al. 2014), determines persistence and that the jets, influenced by meridional temperature gradients, act as waveguides.

Modern ensemble weather prediction on synoptic scales is based on generating an ensemble of deterministic forecasts where the initial perturbation vectors are chosen to

capture flow-dependent information about the deterministic chaotic system i.e. this approach is essentially based on projections onto the low dimensional subspace of the dynamically-relevant growing unstable modes (Pazo et al. 2010). Such modes may grow linearly along directions defined by singular vectors—perturbations with optimal linear growth over a specified time interval (Molteni et al. 1996), or nonlinearly, along bred vectors and generalisations thereof (Toth and Kalnay 1997; O’Kane and Frederiksen 2008; Bowler et al. 2009; O’Kane et al. 2008). As such, modern weather prediction is based on the assumption that the flow is unstable to small perturbations.

Using a combination of one point correlation and the leading EOFs of 300 hPa streamfunction, Branstator (2002) showed that the NH jet stream acts as a waveguide to provide meridional trapping of a zonally elongated wave 5 pattern. Risbey et al. (2015) found a similar circumpolar waveguide pattern via application of FEM-BV-VARX to a suite of atmospheric reanalyses including a high latitude node over northern Europe. They further showed that FEM-BV-VARX could recover all the major empirical indices of the NH teleconnection patterns as well as their secular trends thus providing a unified stochastic modelling framework. In the SH, the circumpolar wave guide has a predominantly wave 3–wave 5 pattern due to the ever present polar jet and the establishment of the winter time subtropical jet. Freitas and Ambrizzi (2012) showed the impact of changes in Hadley Cell intensity on stationary Rossby wave propagation in the SH extratropics including the zonal wave 3 Pacific South American (PSA) wave train emanating from the subtropical central-west Indian Ocean across to the north of South America within the polar jet. Ding et al. (2012) postulated that the link between the Southern Annular Mode (SAM) and the PSA in the Pacific is due to the forced response to tropical SST anomalies manifesting as a geographically fixed active Rossby wave source to the east of Australia within the core of the subtropical jet.

O’Kane et al. (2013) applied the FEM-BV-VARX to the low resolution NCEP v1 reanalysis data set encompassing the period 1948–2009. They characterised the changes in the metastability of the Southern Hemisphere 500-hPa circulation as a regime transition from a period prior to 1978 dominated by switching between positive and negative phases of a hemispheric midlatitude wave 3 blocking state to one post-1978 where there is a strong secular trend toward the positive SAM phase which replaces the negative phase of the hemispheric wave 3 pattern to be the preferred metastable state. Franzke et al. (2015) applied the FEM-BV-VARX to systematically attribute these secular trends using both the NCEP v1 reanalysis and observational radiative forcing data from all seasons. They showed observational evidence that anthropogenic greenhouse gas concentrations have been the major driver of these secular trends in the SAM and blocking

when all seasons are considered, suggesting that the recovery of the ozone hole might delay the signal of global warming less strongly than previously thought.

Here we are interested to examine the high resolution JRA-55 reanalysis in order to try to resolve coherent structures within the subtropical jet and to identify secular trends over recent decades. We are particularly interested to consider systematic changes in stationary Rossby wave propagation and their regional sources, including the role of tropical SSTs as compared to the spatial and temporal characteristics of baroclinic instability over recent decades. We consider the respective roles of meridional temperature gradients and topography on the position of the waveguides, on sources of stationary Rossby waves and their propagation, on the spatio-temporal characteristics of coherent structures in relation to the nodes of the circumpolar waveguide and on the role of barotropic instability through the generation of anomalous potential vorticity. We further examine the flux of pseudo-momentum and infer changes in convection through the velocity potential. We employ a comprehensive set of diagnostics on both isentropic and isobaric surfaces applied to the full SH as well as to the major regions corresponding to the Pacific, Australian–New Zealand, Indian and South American sectors.

The structure of the paper is as follows: The FEM-BV-VARX method and computational details are described in Sect. 2. The reanalysis data and diagnostics are described in Sect. 3. The results, discussion, summary and conclusions are in Sects. 4 and 5 respectively.

2 Method

Although relatively recently developed, the Finite Element Bounded Variation Vector Auto-Regressive with eXternal factors (FEM-BV-VARX) method is now well documented (Horenko 2009; Metzner et al. 2012) and proven in the literature to be of utility in application to the mid-latitude atmosphere (Horenko 2010a, b, c; O’Kane et al. 2013; Risbey et al. 2015; Franzke et al. 2015) and boundary layer (Vercauteren and Klein 2014). Here we provide only a brief outline of the method and refer interested readers to the citations provided. We apply the FEM-BV-VARX analysis to the full Southern Hemisphere region and to a set of regional sectors broadly corresponding to those where well defined atmospheric teleconnections are known to occur e.g. blocking and the PSA for example. We apply the FEM-BV-VARX to daily observational (reanalysis) 500 hPa geopotential height anomalies— $Z'_{g500\text{hPa}}$ —calculated as deviations from the daily climatological mean. The dimensionality of the $Z'_{g500\text{hPa}}$ data is reduced using principal component analysis (PCA) from which the leading twenty PCs are taken. Previous studies have shown that

this reduction is sufficient to characterise the persistent teleconnections of the tropospheric circulation (O’Kane et al. 2013; Risbey et al. 2015).

Here we apply PCA only to reduce the dimensionality of the data. We make no use of the spatial EOF patterns and so avoid the problems associated with questions of stationarity. In principle as long as we have considered sufficiently many modes to capture the underlying dynamics of the large scale atmospheric patterns and assuming that the unresolved scales can be approximated by a stochastic term then our analysis should be robust. In fact O’Kane et al. (2013) have shown that the leading nine modes are sufficient to capture the annular mode and midlatitude coherent blocking structures. At issue is whether we can represent the unresolved modes by a stochastic noise term that projects onto the resolved scales. A further complication is that inclusion of more PCs renders the problem increasingly ill-posed given the length of data available. Here we make the pragmatic choice to limit the dimensionality to 20 PCs. From our calculations with 20 PCs the more crucial issue was being able to use a sufficiently large number of annealing steps.¹

The FEM-BV-VARX approximates dynamical processes by a stochastic model of the form:

$$x_t = \mu_t + A(t)\phi_1(x_{t-\tau}, \dots, x_{t-m\tau}) + B(t)\phi_2(u_t) + C(t)\epsilon_t \quad (1)$$

where $\Theta(t) = (\mu(t), A(t), B(t), C(t))$ is the vector of time dependent model parameters with mean $\mu(t)$. ϕ_1 is in general a nonlinear function connecting present and past observations $(x_{t-\tau}, \dots, x_{t-m\tau})$, but here we take it to be the linear autoregressive factor model. $\phi_2(u_t)$ is an external factor function, and $C(t)$ couples the non-parametric, independent and identically-distributed (i.i.d.) noise process ϵ_t to the analysed time series (hereby modelling the impact of unresolved subgrid-scale effects). Time dependence of the

model parameters $\Theta(t)$ is also induced by the influence of the unresolved scales and leads to regime transitions in many realistic systems. While a posteriori inspection of residuals histograms showing log-normal distribution validates this a priori assumption, it is important to point out that the assumption of “white” noise is made for convenience and is not an a priori requirement for applying the FEM-BV-VARX method.

Importantly and specifically we refer not to the unconditional probability to describe the data by the model i at time t (that would indeed require going through all times between 0 and T) but the conditional one, measuring this probability just at time t when all other information at all other time instances t' are kept fixed. For a given number, K , of clusters and fixed maximal time lag, m , the method minimises the distance of the model trajectory (of model metric g) at each time, t , to one of K model clusters. The model affiliation vector

$$\Gamma(t) = \gamma_1(t), \gamma_2(t), \dots, \gamma_K(t) \quad (2)$$

of time dependent weights is such that the model distance function $g(\cdot)$ can be expressed as a linear combination of local model distance functions. No explicit assumptions on the parametric form of observables distributions are made. The only assumption is that a scalar process describing the time-dependent error of the inverse problem is i.i.d.²

¹ More generally FEM-BV-VARX is formulated to expressly deal with the presence of unresolved external covariates (that are not statistically-independent or identically distributed). Such covariates may result in the non-stationarity and non-homogeneity of the resulting data-driven statistical models and may manifest in the presence of secular trends and/or in regime-transition behavior. By covariate we not only mean external forcings (for a more complete discussion see the companion paper by Franzke et al. 2015) but also unresolved physical processes and scales such as due to EOF truncation. This may then introduce problems when applying the standard stationary approaches common to machine learning and statistics (Wiljes et al. 2014). In the context of this paper, this issue plays a very important role when analyzing atmospheric data since many of the potentially-relevant covariates might not be available explicitly in the set of covariates that we have chosen for testing. Therefore, when deploying statistical time series analysis methods, they should be capable of dealing with non-stationarity and non-homogeneity issues that emerge in the models as a result of these systematically-missing (and potentially-important) external influences.

² In the context of the application of FEM-BV-VARX to the attribution of observed Southern Hemisphere circulation trends to external forcing and internal variability using atmospheric reanalysis data and observed forcing data we have undertaken substantive test of the applicability of AIC. Specifically application of the AIC is equivalent to assuming that the scalar-valued squared model errors are χ^2 -distributed and that the vector-valued FEM-BV-VARX model errors are Gaussian i.e. dependent on the residuals having a log-normal distribution. This assumption was tested using a non-parametric information-theoretic algorithm from Metzner et al. (2012) and found that for all of the model errors ϵ_t the most optimal parametric family was indeed the log-normal distribution. Additionally the log-normal distribution was fitted to the model errors, the respective log-likelihoods computed and used to calculate the AIC for the non-stationary models. Comparable results were found using Akaike Information Criteria Corrected (AICc) and the Bayesian Information Criteria (BIC). The two latter criteria take also the size of the statistics into account and are derived under very different mathematical assumptions than the AIC. This further confirmed our results, demonstrating that they are not induced by the implicit assumptions necessary for the information criteria applicability. Results based on analysis of secular trends in the Southern Annular Mode and planetary wave-3 from the NCEP V1 reanalysis and observed external covariates published in Franzke et al. (2015), show the most informative nonstationary model that emerged using the AIC criteria (with posterior probability almost equal to one in each case) when all seasons are considered was the model with CO2 and memory of 3 days. A similar analysis of the JRA55 reanalysis (unpublished) shows CO2 to be the major driver of the observed secular trends in the subtropics in general agreement with the modelling study of Freitas et al. (2015).

Following Horenko (2011) we will assume that for any $t \in [0, T]$ the global time-dependent (non-stationary) model distance functional $g[\mathbf{x}_t, \boldsymbol{\theta}(t)] : \Psi \times \Omega \rightarrow [0, \infty)$ can be represented as a convex linear combination of $K \geq 1$ stationary model distance functionals—that is, model functionals dependent on some constant (time-independent) local model parameters $\theta_i \in \Omega, i = 1, \dots, K$ chosen according to some time-dependent probabilities (or model affiliations) $\Gamma(t)$. $\Gamma(t)$ together with $\theta_1, \dots, \theta_K$ are jointly obtained from the numerical optimisation given by Eq. 3. The method treats the clustering of non-stationary multidimensional data, $x_t \in R^d$ as a minimisation problem:

$$L(\Theta, \Gamma) = \sum_{t=0}^T \sum_{i=1}^K \gamma_i(t) g(x_t, u_t, \theta_i) \rightarrow \min(\Gamma(t), \Theta) \quad (3)$$

subject to convexity constraints $\sum_{i=1}^K \gamma_i(t) = 1, \forall t \in [0, T]$ and $\gamma_i(t) \geq 0, \forall t \in [0, T], i = 1, \dots, K$.

To select the proper order parameters for the VARX model, the optimal functional for external factors in Eq. 1 and to account for parsimony we apply information theoretic criteria. Specifically, we apply the Akaike Information Criteria (Akaike 1988) to assess the goodness of fit relative to the number of fitted parameters or external factors used, allowing one to find the model that is least over-fitting while best fitting the analysed data. In practice the lowest Akaike Information Criterion (AIC) value is chosen, where $AIC = -2\log L_{max} + 2M$ with L_{max} the maximum log likelihood achievable by the model and M the number of free parameters. The optimal model for the number of clusters, K , with a given persistency threshold determined in this way is the best fitting model with the fewest free parameters (Metzner et al. 2012).

The number of different spatio-temporal clusters K , the model parameters to be chosen, such as memory depth and number of PCs, and the indicator functions $\gamma_k(\cdot)$ signalling activation of the respective models, are all determined simultaneously in a global optimisation procedure. This yields a judicious compromise between low residuals in reproducing the data of a training set on the one hand, and the demand for the smallest-possible overall number of free parameters of the complete model on the other. The resulting FEM-BV-framework is essentially parameter free apart from the overall number of optimisation repetitions (annealing steps) with different randomly-chosen initial values Γ or Θ for parameter optimisation. Increasing this number reduces the probability of getting trapped in one of the local minima of L (for $N_C > 0$), simultaneously linearly increasing the amount of computations. Therefore, the number of annealing steps should be chosen carefully, dependent on the available computational

resources and the size of the data to be analysed. We have considered 4, 8, 16, 32, 64, 128 and 256 annealing steps in order to rigorously test sensitivity to this parameter choice. We found qualitative agreement between 64, 128 and 256 annealing steps with 256 representing the limits of our computational resources. We show only results for 256 annealing steps and the FEM-BV-VARX conducted using $Z'_{g, 500 \text{ hPa}}$ data.

A key output of the FEM-BV-VARX method is the posterior model affiliation sequence (or Viterbi path) describing the most likely cluster state, i , of the system at each time. From the Viterbi path one can construct composites by averaging x , here corresponding to 500 hPa anomalies, over all times when the system is in each of the respective cluster states $i = 1, \dots, K$. Specifically the i th composite here is the average of state space vectors x conditioned on $\gamma_i(t) = 1$ and conditioned on the season or annually as appropriate. For each of our domains, $K = 2$ cluster states were obtained, corresponding to the positive and negative phases of the dominant quasi-stationary teleconnection modes. The composites show the spatial structure of each metastable state. The Viterbi path also allows a construction of the residence behaviour of the system in switching between each cluster state and allows for the identification of secular trends. Composites for each metastable state were constructed for each of the seasons (DJF, MAM, JJA, SON) and for a comprehensive set of diagnostic variables.

3 Data and diagnostics

3.1 JRA-55 reanalysis

We analyse the Japanese 55-years Reanalysis (JRA-55) conducted by the Japan Meteorological Agency (JMA). JRA-55 covers the global radiosonde period from 1958 through to 2013 and is the first to apply four-dimensional variational analysis to this period. The JRA-55 was carried out with the express goal *to address issues found in previous reanalyses and to produce a comprehensive atmospheric dataset suitable for studying multidecadal variability and climate change*. Details of the JRA-55 are described by Kobayashi et al. (2015) including the observations assimilated, data assimilation system, and forecast model including the basic characteristics of the JRA-55 product. JRA-55 was produced with JMA's operational data assimilation system at TL319 resolution with major improvements including a reduced cold bias in the lower stratosphere and a mitigated dry bias in the Amazon basin. We found our results were generally replicated in sensitivity studies using $Z_{g, 500 \text{ hPa}}$ fields from the ERA interim reanalysis which is of comparable resolution to JRA-55.

3.2 Diagnostics

In order to examine the dynamics of persistent states identified using the FEM-BV-VARX framework we employ a comprehensive set of diagnostics, applied to daily mean data on both isentropic and isobaric surfaces. Specifically, we consider on the 500 hPa isobaric pressure surface, streamfunction $\psi_{500\text{hPa}}(\text{m}^2\text{s}^{-1})$, eddy streamfunctions in terms of the deviation from the zonally averaged streamfunction $\psi_{500\text{hPa}}^{\text{eddy}}(\text{m}^2\text{s}^{-1})$ and geopotential height $Z_{g,500\text{hPa}}(\text{m})$. On the 300 hPa isobaric pressure surface, we consider u-winds $u_{300\text{hPa}}(\text{m}\text{s}^{-1})$, velocity potential $\chi_{300\text{hPa}}(\text{m}^2\text{s}^{-1})$ and divergent winds $\mathbf{v}_{\chi,300\text{hPa}}(\text{m}\text{s}^{-1})$, Rossby wave source $RWS_{300\text{hPa}}(\text{s}^{-2})$ and wave activity flux $\mathbf{W}_{300\text{hPa}}(\text{m}^2\text{s}^{-2})$. As a measure of baroclinic instability, we calculate the Phillips criterion PCr at 300–700 hPa (ms^{-1}). On the 320 K isentropic θ surface, we examine potential vorticity $PV_{320\text{K}}(\text{m}^2\text{s}^{-1}\text{K}\text{kg}^{-1})$. Unless otherwise stated all anomalies are w.r.t. the daily climatological mean i.e. deviations from the daily climatological mean value for the period 1958–2013 inclusive. In the following sections we describe the diagnostic utility of each.

3.2.1 Geopotential height, streamfunction and potential vorticity

Geopotential height has units of meters and is defined as $Z_g = gz$, where g is gravity and z the vertical coordinate in the direction normal to the geopotential surface (Vallis 2010). Here, we will consider Z_g on the 500 hPa surface i.e. $Z_{g,500\text{hPa}}$, as this represents the middle of the troposphere. The streamfunction is related to the relative vorticity by the Laplacian $\zeta = \nabla^2\psi$ and is a measure of the large scale flow. Hoskins (1991) referred to the region of the tropopause between the 270 and 380 K isentropes as the “Middleworld”, where Rossby waves can couple giving rise to baroclinic instability. Here, we consider potential vorticity on the 320 K isentrope i.e. $PV'_{320\text{K}}$. Liniger and Davies (2004) (their Fig. 1) show that, for the climatological Northern winter, the 300 hPa pressure and 310–320 K θ -potential temperature isentropes intersect with the $2PVU = 2 \times 10^{-6}\text{m}^2\text{s}^{-1}\text{K}\text{kg}^{-1}$ surface, otherwise referred to as the dynamic tropopause, at $\approx 45^\circ\text{N}$ latitude. In the SH, this intersection undergoes a significant meridional displacement from the subtropics in the winter to high latitudes in the summer consistent with the splitting of the wintertime midlatitude jet.

3.2.2 Phillips criterion

As a simple diagnostic for incipient baroclinic instability, we apply the Phillips Criteria (PCr) (Phillips 1954) in terms of the shear between the horizontal winds u at 300 and 700 hPa as

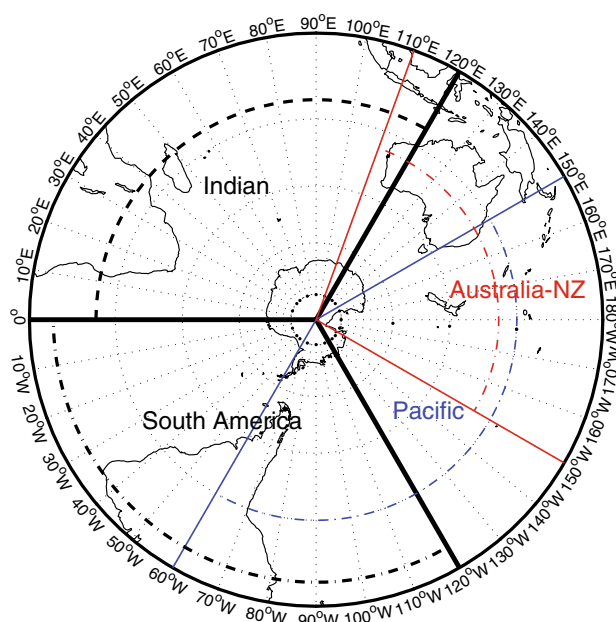


Fig. 1 Diagram of sectors on which the FEM-BV-VARX is applied. Including the full hemisphere $0^\circ\text{--}360^\circ$, sectors are considered in an anti-clockwise direction starting with the Australian–New Zealand sector $150^\circ\text{W}\text{--}110^\circ\text{E}$, Indian sector $120^\circ\text{E}\text{--}0^\circ$, South American sector $0^\circ\text{--}120^\circ\text{W}$ and finally the Pacific sector $60^\circ\text{W}\text{--}150^\circ\text{E}$

$$PCr = \bar{u}^{300} - \bar{u}^{700} - \frac{b_\kappa c_p \bar{\sigma}}{a\Omega} \frac{\cos\phi}{\sin^2\phi} \geq 0, \tag{4}$$

where $\bar{\sigma}$ is the static stability for a given basic (climatological) state, typically calculated as $1/2(\theta^{300} - \theta^{700})$ where θ is the potential temperature at 300 and 700 hPa. $c_p = 1004\text{J deg}^{-1}\text{kg}^{-1}$, is the specific heat of air at constant pressure, $\Omega = 7.292 \times 10^{-5}\text{rad s}^{-1}$, is the earth’s angular speed of rotation, $b_\kappa = 0.124$ is a dimensionless constant, $a = 6.371 \times 10^6\text{m}$, is the radius of the earth and ϕ is latitude. Positive values are indicative that the flow is unstable to small perturbations i.e. that the mid-tropospheric atmosphere is unstable to storm development. In addition we will consider the anomalous PCr w.r.t. its daily climatological values. PCr is in units of ms^{-1} .

3.2.3 Velocity potential and Rossby wave source

The velocity potential χ (units m^2s^{-1}) describes the divergent irrotational part of the horizontal velocity field \mathbf{v} via the Poisson equation $\nabla \cdot \mathbf{v} = \nabla^2\chi$ (Lynch 1988). Negative upper level velocity potential values are indicative of diverging winds and rising air whereas positive values identify regions of converging winds and subsiding air beneath. Anomalous positive (negative) values are indicative of weak (deep) convection and reduced (enhanced) precipitation respectively. Divergent winds are indicated by the vector components of $\mathbf{v}_\chi = \nabla\chi$.

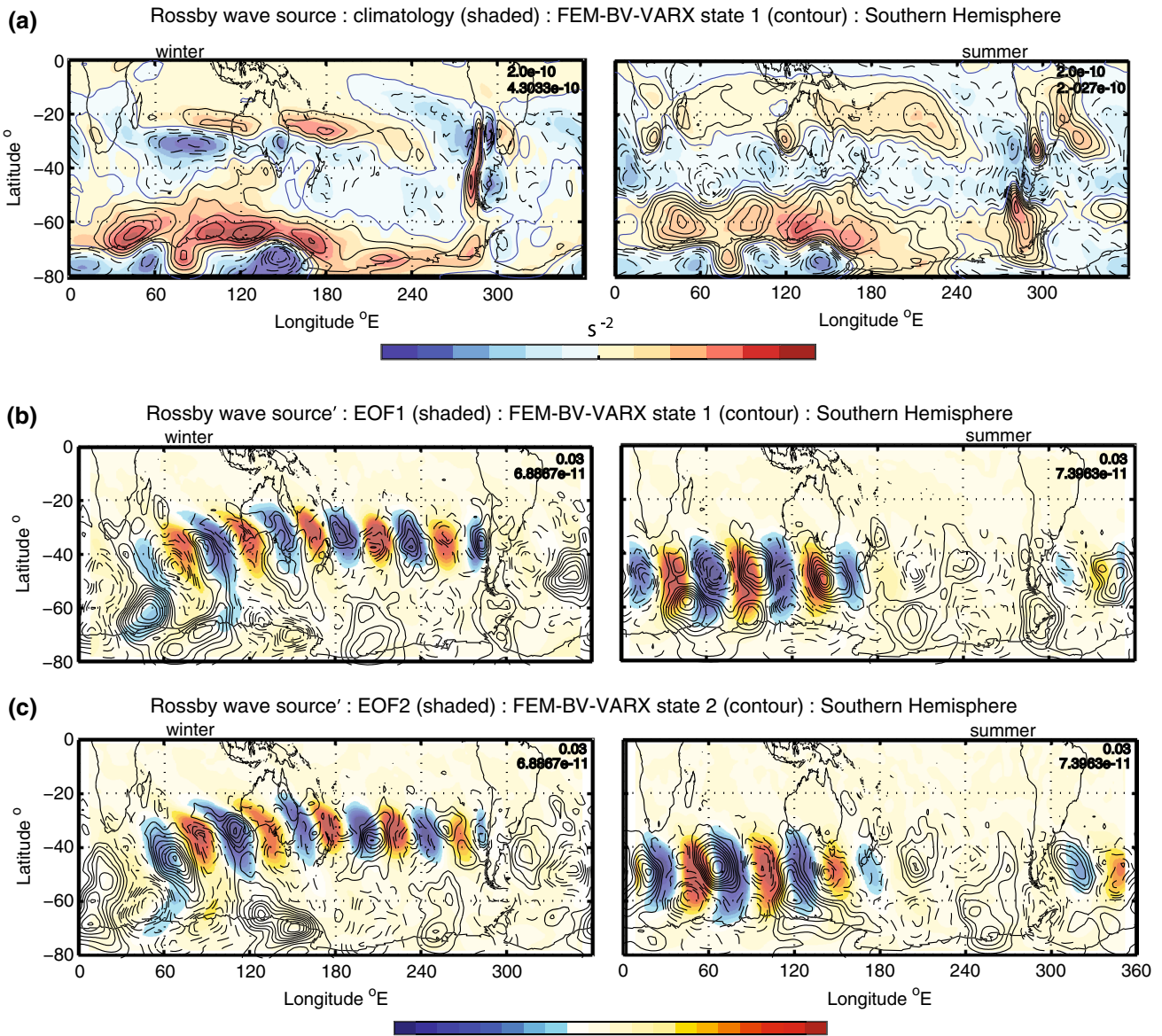


Fig. 2 A comparison of FEM-BV-VARX composite (stationary) states to an EOF analysis of RWS_{300hPa} over the SH. **a** Climatological RWS_{300hPa} (shaded) and FEM-BV-VARX RWS_{300hPa} state 1 (contours) in winter and summer in units of s^{-2} . **b, c** Leading two EOF patterns corresponding to the dominant propagating RWS_{300hPa} mode in winter and summer (shaded). FEM-BV-VARX states 1 and 2 for the anomalous RWS'_{300hPa} (contours). All fields are centred with the

shaded fields coloured according to the colour bars shown. The contoured fields (solid—positive values; dashed—negative values) are partitioned according to the lower colour bar partitions and the max (min) values for the shaded (top value) and contoured (bottom value) fields are shown in the top right corner of each of the panels. Unless indicated otherwise, in all figures to follow we will use this labelling convention

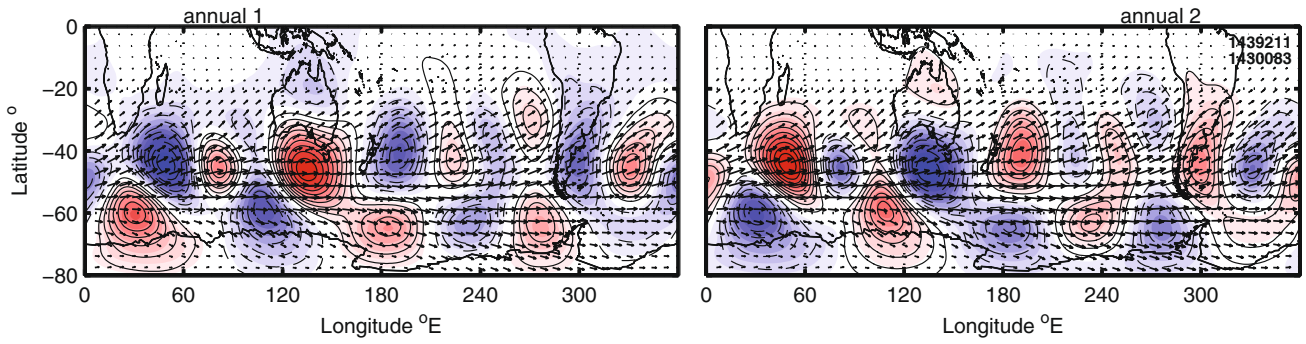
Sardeshmukh and Hoskins (1988) used the RWS to examine the mechanisms by which the mid-latitude circulation might respond to changes associated with tropical convection. The RWS may be simply derived from the barotropic vorticity equation as follows:

$$\left(\frac{\partial}{\partial t} + \mathbf{v} \cdot \nabla\right)\zeta = -\zeta \nabla \cdot \mathbf{v} \quad (5)$$

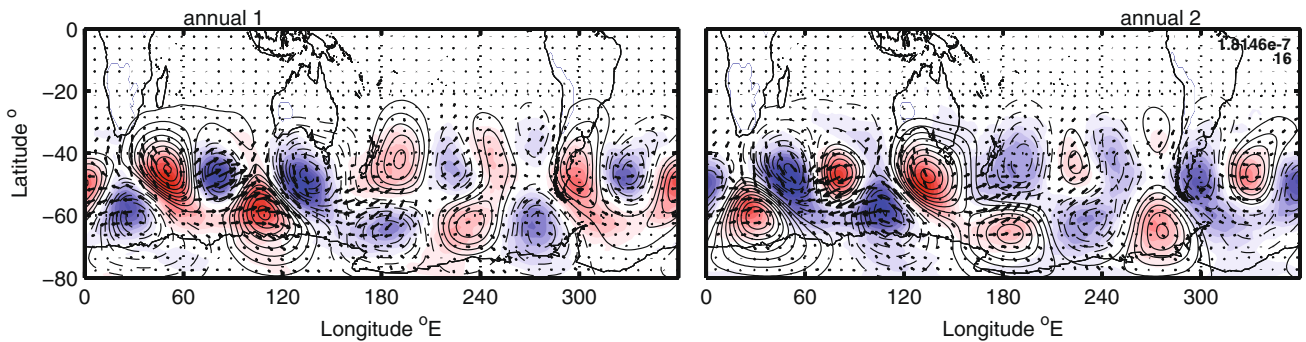
where ζ is the absolute vorticity i.e. $\zeta = \xi + f$ where ξ is the relative vorticity and f is the Coriolis parameter. \mathbf{v} is the wind velocity vector and ∇ is the gradient operator. Now by the Helmholtz theorem the wind velocity vector can be decomposed in terms of its divergent (irrotational) component, obtained from the velocity potential χ , and rotational terms i.e.

$$\mathbf{v} = \nabla\chi + \mathbf{k} \times \nabla\psi \quad (6)$$

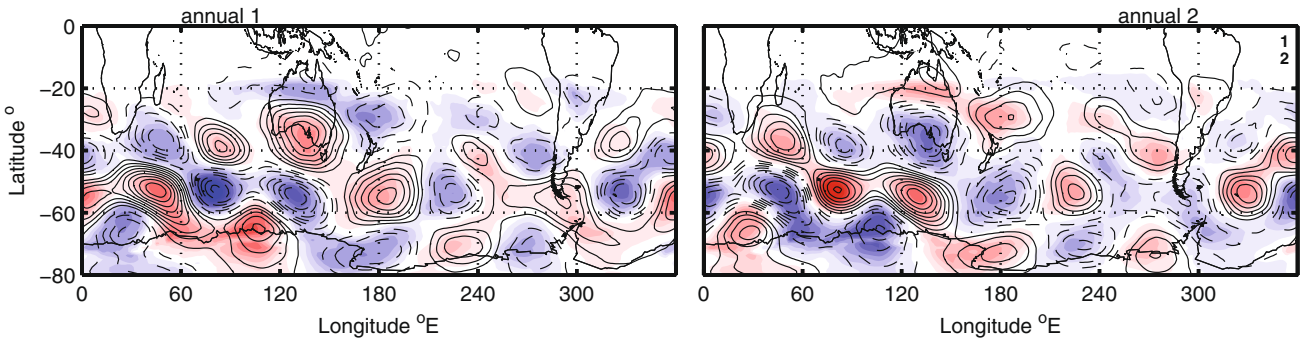
(a) streamfunction' 500hPa (shaded) : eddy streamfunction' (contours) : wave activity flux (vectors) : Southern Hemisphere



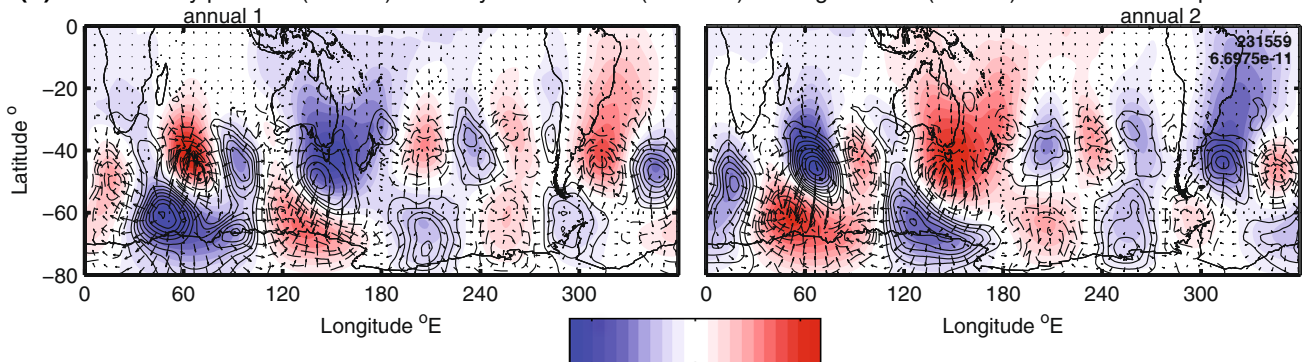
(b) potential vorticity'(shaded) : 500hPa geopotential'(contours) : wave activity flux'(vectors) : Southern Hemisphere



(c) Phillips criterion (shaded) : u-wind' (contours) : Southern Hemisphere



(d) velocity potential'(shaded) : Rossby wave source' (contours) : divergent wind' (vectors): Southern Hemisphere



◀ **Fig. 3** Annual composites based on the FEM-BV-VARX model affiliation sequence. All fields are *centred* and *shaded/contoured* according to the *color bar* partitions shown. The max (min) values are shown in the *top right corner* of each panel with the *upper number* corresponding to the *shaded variable* and the *lower* the *contoured variable*. *Dashed lines* indicate negative values. **a** streamfunction anomalies on the 500 hPa isobaric pressure surface $\psi_{500\text{hPa}}$ (*shaded*) units $\text{m}^2 \text{s}^{-1}$, eddy streamfunction anomalies calculated from streamfunction at 500 hPa in terms of zonal asymmetries $\psi_{500\text{hPa}}^{\text{eddy}}$ (*contours*) in units $\text{m}^2 \text{s}^{-1}$ and wave activity flux $\mathbf{W}_{300\text{hPa}}$ (*vectors*) in units $\text{m}^2 \text{s}^{-2}$. **b** Potential vorticity anomalies on the 320 K isentropic θ surface $PV_{320\text{K}}'$ (*shaded*) in units $\text{m}^2 \text{s}^{-1} \text{K kg}^{-1}$, 500 hPa geopotential height anomalies $Z'_{g500\text{hPa}}$ (*contours*) in units m and anomalous wave activity flux $\mathbf{W}'_{300\text{hPa}}$ (*vectors*) on the 300 hPa isobaric surface. **c** Anomalous Phillips criterion PCr' (*shaded*) in units m s^{-1} and anomalous u-winds at 300 hPa $u'_{300\text{hPa}}$ (*contours*) in units m s^{-1} . **d** Anomalous 300 hPa velocity potential $\chi'_{300\text{hPa}}$ (*shaded*) in units $\text{m}^2 \text{s}^{-1}$, anomalous 300 hPa Rossby wave source $RWS'_{300\text{hPa}}$ (*contours*) in units s^{-2} and divergent winds $v'_{\chi300\text{hPa}}$ in m s^{-1}

$$= \mathbf{v}_\chi + \mathbf{v}_\psi \tag{7}$$

then Eq. 5 may be written as

$$\left(\frac{\partial}{\partial t} + \mathbf{v}_\psi \cdot \nabla + \mathbf{v}_\chi \cdot \nabla \right) \zeta = -\zeta [\nabla \cdot \mathbf{v}_\psi + \nabla \cdot \mathbf{v}_\chi] \tag{8}$$

$$\left(\frac{\partial}{\partial t} + \mathbf{v}_\psi \cdot \nabla \right) \zeta = -\zeta \nabla \cdot \mathbf{v}_\chi - \mathbf{v}_\chi \cdot \nabla \zeta \tag{9}$$

$$= -\nabla \cdot (\mathbf{v}_\chi \zeta) \tag{10}$$

as

$$\nabla \cdot \mathbf{v} = \nabla \cdot \mathbf{v}_\chi + \nabla \cdot \mathbf{v}_\psi \tag{11}$$

$$= \nabla \cdot \mathbf{v}_\chi \tag{12}$$

where the divergence of the rotational wind component is zero.

The *RWS* (units s^{-2}) is simply defined as the RHS of Eq. 10. In component form this is

$$RWS = - \left[\zeta \frac{\partial}{\partial x} \mathbf{v}_\chi \mathbf{i} \cdot \mathbf{i} + \zeta \frac{\partial}{\partial y} \mathbf{v}_\chi \mathbf{j} \cdot \mathbf{j} \right] - \left[\mathbf{v}_\chi \mathbf{i} \cdot \frac{\partial \zeta}{\partial x} \mathbf{i} + \mathbf{v}_\chi \mathbf{j} \cdot \frac{\partial \zeta}{\partial y} \mathbf{j} \right] \tag{13}$$

$$= -\zeta \left[\frac{\partial u}{\partial x} + \frac{\partial v}{\partial y} \right] - \mathbf{v}_\chi \cdot \nabla \zeta \tag{14}$$

where the first term on the RHS of Eq. 14 is the vortex stretching term describing the generation of vorticity by the horizontal divergence, whereas the second describes the advection of absolute vorticity by the divergent flow.

The *RWS* is largest in regions where divergent winds and gradients in absolute vorticity are largest. As discussed by Shimizu and de Albuquerque Calvalcanti (2011), this may occur in the jet stream regions where large gradients in

vorticity occur or poleward of diabatic tropical heating. In the SH, negative (positive) values indicate cyclonic (anticyclonic) Rossby wave sources and convergence (divergence). Similar to Freitas and Ambrizzi (2012), we will further consider the time evolving anomalous *RWS* as being due to the anomalous divergence w.r.t. the daily climatological mean i.e. $RWS' = RWS - \langle RWS \rangle$. This approach differs somewhat from that of Sardeshmukh and Hoskins (1988), who considered linearised dynamics about a mean ambient flow i.e. $RWS' = -\nabla \cdot (\mathbf{v}'_\chi \bar{\zeta}) - \nabla \cdot (\bar{\mathbf{v}}_\chi \zeta')$.

3.2.4 Wave activity flux

Plumb (1986) first analysed the zonal propagation of transient eddies embedded on a zonally asymmetric basic state i.e. propagation of a wave packet relative to the time-mean flow, defining an equation for the flux of wave activity pseudomomentum. This approach is based on a conservation law representing three-dimensional wave propagation, where the wave-activity flux is free from any oscillatory component (Plumb 1985), and has been routinely applied to analyse large scale stationary disturbances in the troposphere e.g. (Karoly et al. 1989). We consider the horizontal components of the wave activity flux vector based on the daily climatological horizontal wind vector components *U* and *V* and the anomalous stream function at 300 hPa, using the more general formulation described by Takaya and Nakamura (2001) and applicable for either stationary or migratory quasigeostrophic eddies on a zonally varying basic flow. i.e.

$$\mathbf{W} = \frac{1}{2|\mathbf{U}|} \left[(U(\psi_x'^2 - \psi' \psi_{xx}') + V(\psi_x' \psi_y' - \psi' \psi_{xy}')) \mathbf{i} + (U(\psi_x' \psi_y' - \psi' \psi_{xy}') + V(\psi_y'^2 - \psi' \psi_{yy}')) \mathbf{j} \right]. \tag{15}$$

Here we use \mathbf{W} (units $\text{m}^2 \text{s}^{-2}$) to analyse the instantaneous propagation of a wave packet associated with both stationary and migratory eddies in the observed mid-tropospheric flow. An important point is that the formulation of Takaya and Nakamura (2001), based on an approximate conservation relation of wave-activity pseudomomentum, allows the clean separation between the climatological time-mean flow and anomalies embedded on it. In the results that follow, we will consider composites of \mathbf{W} according to the posterior model affiliation sequence as determined by the FEM-BV-VARX methodology. We will also show that, as \mathbf{W}' is quadratic and for sufficient sampling (here we are using ≈ 55 years of daily data), the anomalous \mathbf{W}' w.r.t. the climatological daily mean, further allows one to identify regions of divergence and convergence of momentum associated with the rotational component of the flow.

4 Results and discussion

In this section we consider the manifestation of quasi-stationary persistent states in the SH and in each of the regional sectors defined in Fig. 1. In the figures and discussion that follows ‘ indicates anomaly from the daily climatological mean. For each of the sectors the composites, generated from the posterior model affiliation sequence from the respective FEM-BV-VARX sector calculations, are displayed on the full hemispheric domain.

4.1 SH circumpolar and subtropical waveguides

Branstator (2002) showed that the Northern Hemisphere (NH) jet stream acts as a waveguide allowing the meridional trapping of disturbances that can become zonally elongated and teleconnected around the hemisphere. Risbey et al. (2015) showed that the FEM-BV-VARX cluster states for the Northern Hemisphere domain (their Fig. 7) exhibit a midlatitude waveguide, spanning much of the hemisphere and displaying a wave 5 pattern in the jetstream waveguide, with a high latitude node over northern Europe, closely corresponding to the circumpolar waveguide pattern (CWP) mode identified by Branstator (2002). Here we focus on the SH circumpolar waveguide pattern.

In order to illustrate the utility of the nonstationary data analysis method to more standard approaches, we compare FEM-BV-VARX states of $RWS_{300\text{hPa}}$ composited over the entire reanalysis period from the model affiliation sequence. For ≈ 55 years of daily data, these states are close to the spatial patterns of the stationary states and can be compared to an EOF analysis of $RWS_{300\text{hPa}}$ over the SH. In Fig. 2a, we show seasonal climatological $RWS_{300\text{hPa}}$ (shaded) and FEM-BV-VARX $RWS_{300\text{hPa}}$ state 1 (contours) for the winter and summer. That both are highly-correlated is not unexpected, as we are considering a very large sample of daily data. The real differences emerge when anomalies are examined. In Fig. 2b, c, the leading two EOF patterns, corresponding to the dominant propagating $RWS_{300\text{hPa}}$ mode in winter (left hand panels) and summer (right hand panels), are shown with contours of the FEM-BV-VARX composite states 1 and 2 for the anomalous $RWS'_{300\text{hPa}}$ superimposed. The leading $RWS'_{300\text{hPa}}$ EOF patterns 1 and 2 associated with the RWS analysis show similar wave trains in the subtropics. $RWS'_{300\text{hPa}}$ EOF 1 is 90° out of phase with $RWS'_{300\text{hPa}}$ EOF 2 i.e. in quadrature and the eigenvalues corresponding to $RWS'_{300\text{hPa}}$ EOF 1 and 2 have nearly the same value and are distinct from the remaining eigenvalues.

For the winter, we see that the leading EOF patterns and FEM-BV-VARX $RWS'_{300\text{hPa}}$ states are largely manifested in the subtropical jet. However, the FEM-BV-VARX $RWS'_{300\text{hPa}}$ states show significant structures in the polar jet

and in particular in the Indian Ocean, which are nearly absent from the EOF patterns. For the summer, the leading EOFs of the dominant propagating mode are entirely localised in the Indian Ocean sector. The FEM-BV-VARX $RWS'_{300\text{hPa}}$ states are also largest in this region, but with important differences in the rest of the hemisphere. The point here is that an EOF analysis does not provide the same structural information about the teleconnections as the FEM-BV-VARX methodology. More generally, the EOF patterns are based on maximising the variance and therefore do not necessarily correspond to physical patterns. Principal component analysis (PCA) assumes that the time series is statistically-stationary, does not take into account persistence and so in general cannot provide any reliable information on regimes and their secular trends.

In Fig. 3, we show average composites based on the annual FEM-BV-VARX model affiliation sequence for the SH—these we will refer to as annual composites. Eddy streamfunction anomalies $\psi'_{500\text{hPa}}{}^{\text{eddy}}$ (contours) and wave activity flux $\mathbf{W}'_{300\text{hPa}}$ (vectors) are superimposed onto streamfunction anomalies on the 500 hPa isobaric pressure surface $\psi'_{500\text{hPa}}$ (shaded) (Fig. 3a). Particularly evident is the splitting of the wave structure in the Pacific with both upper (consistent with the formation of the wintertime subtropical jet) and lower (consistent with the year round polar jet) wavetrains. The upper wave train has a wave-5 structure with the lower having a wave-3 structure. $\psi'_{500\text{hPa}}{}^{\text{eddy}}$ and $\psi'_{500\text{hPa}}$ anomalies are positively-correlated with equivalent structures. $\mathbf{W}'_{300\text{hPa}}$ vectors clearly display the split jet in the Pacific in broad agreement with the waveguide described by Ambrizzi et al. (1995) (their Fig. 17).

It has been suggested that potential vorticity on isentropic surfaces is a more dynamically-relevant diagnostic than streamfunction or geopotential height on isobaric surfaces (Hoskins 2015). Liniger and Davies (2004), argue that the distribution of extratropical potential vorticity on isentropic surfaces that transect the dynamic tropopause ($2PVU$ surface) is a key feature of planetary-scale teleconnection patterns and synoptic-scale weather systems, and can further be used to identify mesoscale stratosphere-troposphere exchanges. In Fig. 3b, we show composite states for anomalies on the 320 K isentropic θ surface $PV'_{320\text{K}}$ (shaded) with 500 hPa geopotential height anomalies $Z'_{g500\text{hPa}}$ (contours) and anomalous wave activity flux $\mathbf{W}'_{300\text{hPa}}$ vectors on the 300 hPa isobaric surface superimposed. $PV'_{320\text{K}}$ and $Z'_{g500\text{hPa}}$ are positively correlated and anti-correlated with $\psi'_{500\text{hPa}}{}^{\text{eddy}}$ and $\psi'_{500\text{hPa}}$ (Fig. 3a) while displaying the same wave structure. $\mathbf{W}'_{300\text{hPa}}$ vectors show regions of positive (negative) $PV'_{320\text{K}}$ and $Z'_{g500\text{hPa}}$ correspond to regions of divergent (convergent) anomalous mass flux.

PCr provides a useful diagnostic for incipient baroclinic instability. Figure 3c shows composite states for anomalous

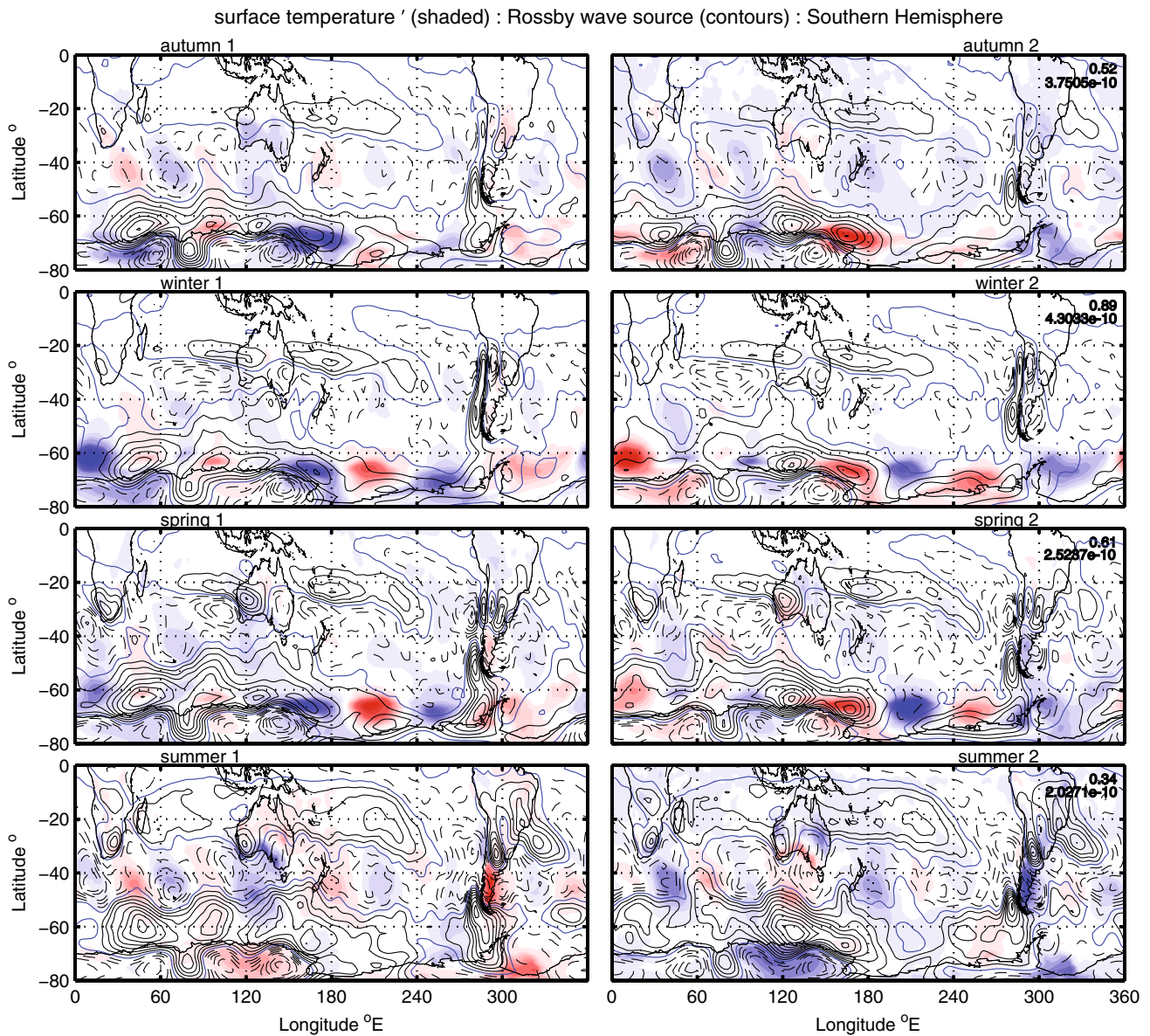


Fig. 4 As for Fig. 3 but for surface temperature anomalies SAT' (shaded) in Kelvin K and $RWS_{300\text{hPa}}$ (contours) in s^{-2} and by season

Phillips criterion PCr' (shaded) and anomalous u-winds at 300 hPa $u'_{300\text{hPa}}$ (contours). As PCr' is simply the difference between the u-winds at 300 and 700 hPa, it is not surprising that the two diagnostics are positively correlated. Of interest are the large gradients in the Indian Ocean between 0°E and 120°E . These structures will be discussed in some detail in Sect. 4.3.

In Fig. 3d, anomalous 300 hPa Rossby wave source $RWS'_{300\text{hPa}}$ contours are superimposed onto the anomalous 300 hPa velocity potential $\chi'_{300\text{hPa}}$ (shaded). We see that the regions of negative (positive) χ are strongly correlated with divergent (convergent) anomalous wind vectors and with large gradients in absolute vorticity associated with anticyclonic (cyclonic) Rossby wave source regions—indicated

by positive (negative) $RWS'_{300\text{hPa}}$. As expected $\chi'_{300\text{hPa}}$ and $\psi'_{300\text{hPa}}$ are in quadrature (Chen and Chen 1997). Here, large gradients in $RWS'_{300\text{hPa}}$ occur at the nodes of the $PV'_{320\text{K}}$ wavetrain with positive (negative) $PV'_{320\text{K}}$ and $Z'_{g500\text{hPa}}$ anomalies, centred about negative–positive (positive–negative) westerly horizontal gradients.

In order to understand the role of meridional temperature gradients, surface air temperatures and topography in Rossby wave breaking—as well as the generation of persistent anomalies—we compare SAT' anomalies and $RWS_{300\text{hPa}}$ (Fig. 4). In the winter and spring we see significant SAT' anomalies along the Antarctic coastline and extending equatorward to 60°S associated with the formation of ice. In the summer, and to a lesser extent in the

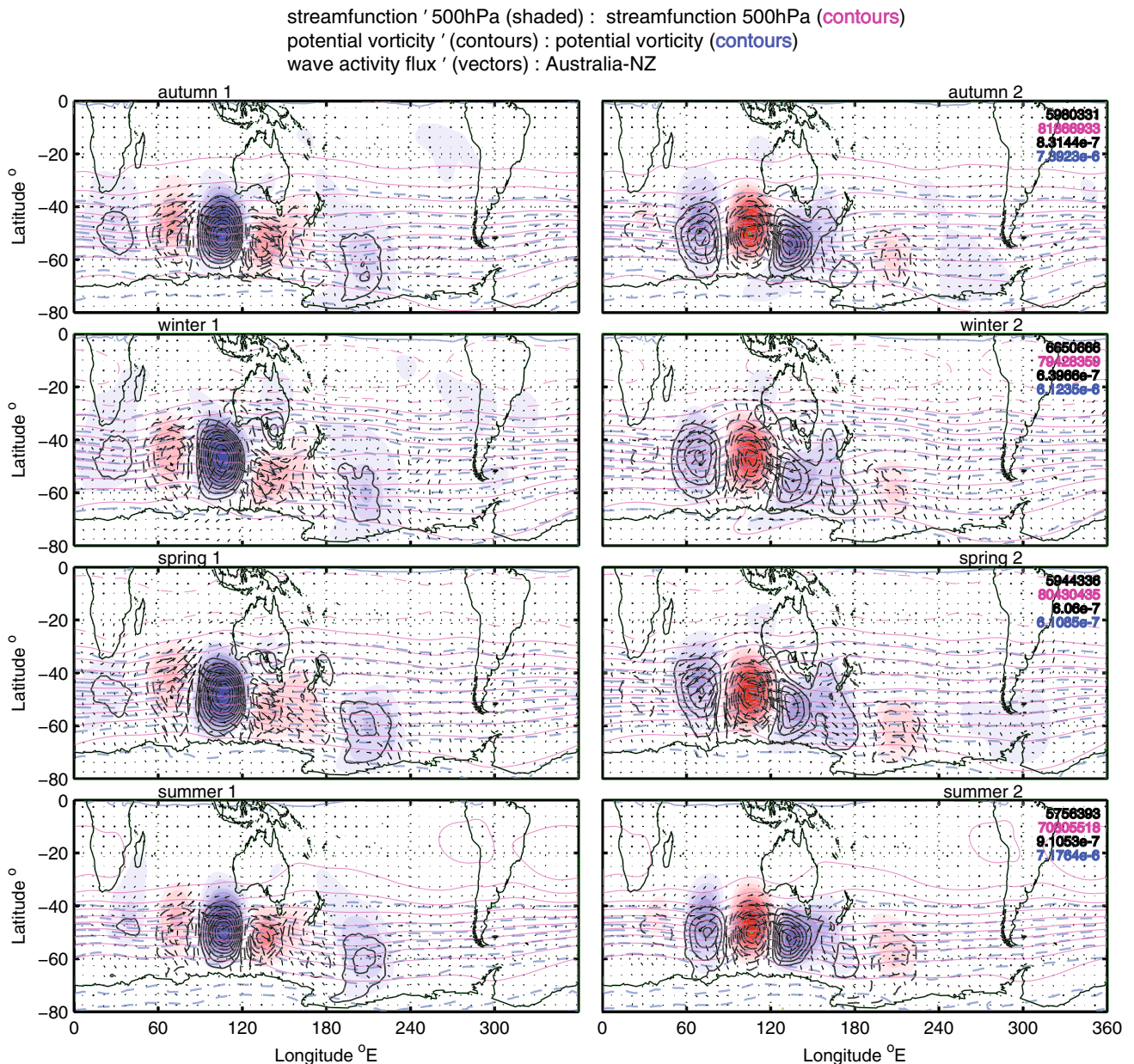


Fig. 5 Seasonal FEM-BV-VARX composite states 1 and 2 for the Australian–NZ sector $\psi'_{500\text{hPa}}$ (shaded) and $\psi'_{500\text{hPa}}$ (magenta contours), $PV'_{320\text{K}}$ (contours), $PV'_{320\text{K}}$ (blue contours) and $W'_{300\text{hPa}}$ (vectors). All fields are centred and shaded/contoured according to the color bar shown in Fig. 2 with the max/min values shown in the

autumn, SAT' anomalies occur in the midlatitude band confined to a broad region of negative $RWS'_{300\text{hPa}}$ where significant $RWS'_{300\text{hPa}}$ anomalies occur. In the summer negative (positive) SAT' anomalies are coincident with large scale cyclonic (anticyclonic) $PV'_{320\text{K}}$ and $Z'_{g500\text{hPa}}$ anomalies indicating the importance of Indian Ocean meridional temperature gradients in the summertime circulation. From these results it appears that SAT' anomalies, in particular at the Indian Ocean midlatitudes, are an important source

of Rossby waves in the summer and autumn. On the other hand topographic features and the Andes in particular, dominate winter–spring Rossby wave sources. In the sections that follow, we will return to this topic.

4.2 Australia–NZ sector

Next, we examine persistent states based on FEM-BV-VARX composites calculated for the Australian–NZ sector

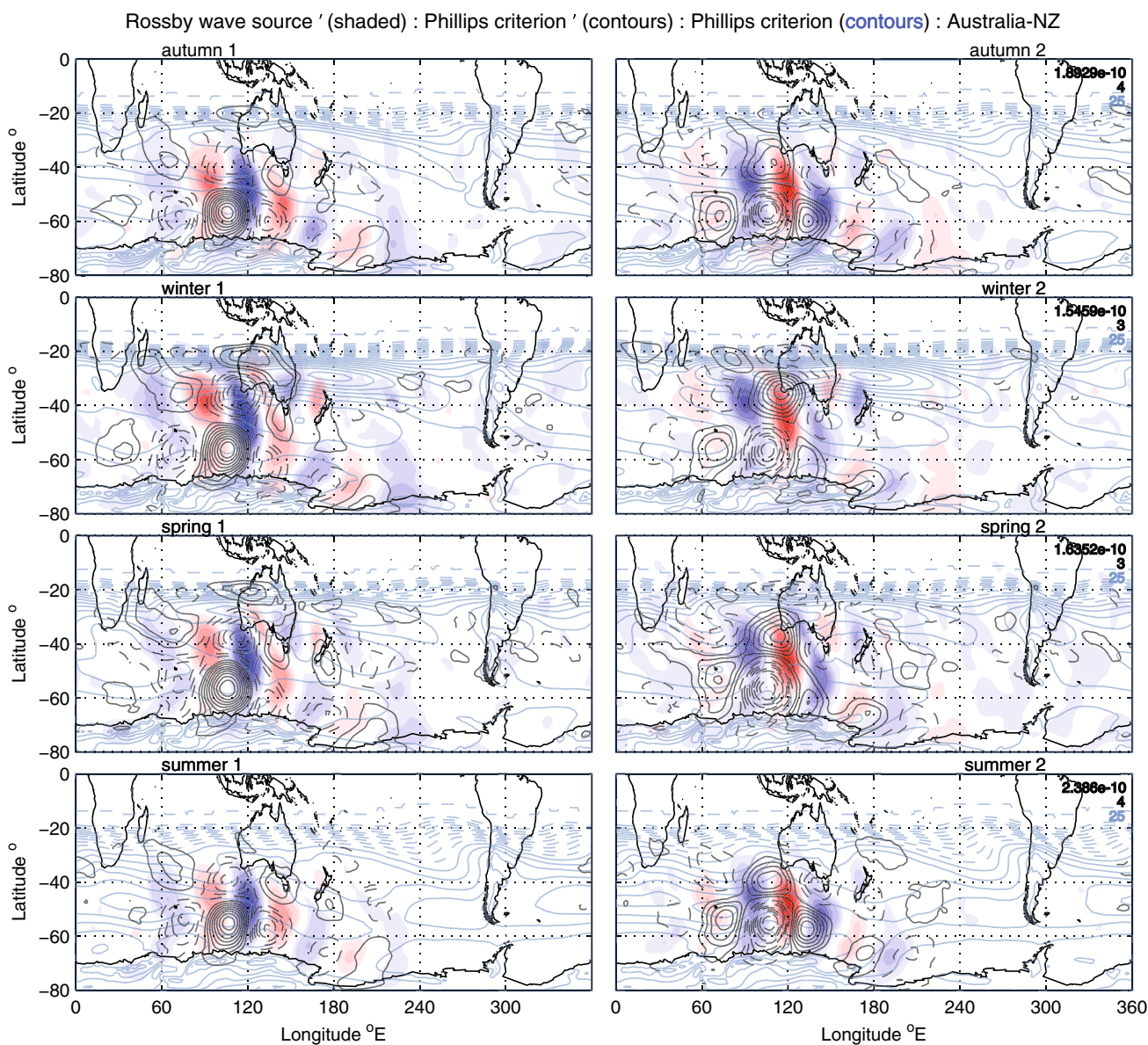


Fig. 6 As for Fig. 5 but for $RWS'_{300\text{hPa}}$ (shaded), PCr' (contours) and PCr (blue contours)

between 150°W and 110°E . In Fig. 5, we see a wavetrain confined to the midlatitude band between about 40°S and 60°S for both $PV'_{320\text{K}}$ and $\psi'_{500\text{hPa}}$. The nodes of the $PV'_{320\text{K}}$ wavetrain are anticorrelated with and slightly displaced poleward relative to those of the $\psi'_{500\text{hPa}}$ wavetrain, consistent with the mean $PV_{320\text{K}}$ and $\psi_{500\text{hPa}}$ meridional gradients. For the midlatitudes, these diagnostics reveal largely the same information. The wintertime wavetrain is meridionally extended relative to a distinctly contracted summertime pattern. The anomalous $\mathbf{W}'_{300\text{hPa}}$ flux is in quadrature with and moving predominantly in an anticlockwise (clockwise) direction for regions of positive–negative (negative–positive) $\psi'_{500\text{hPa}}$ in FEM-BV-VARX state 1 (state 2).

A comparison of $RWS'_{300\text{hPa}}$ (Fig. 6) again shows a midlatitude wavetrain with positive–negative (negative–positive) structures occurring in regions of positive (negative) $PV'_{320\text{K}}$ anomalies. This is indicative of wave breaking occurring where Rossby waves encounter persistent anticyclonic $Z'_{g500\text{hPa}}$ anomalies, generating potential vorticity which in turn acts to maintain the anomaly (Luo et al. 2014). Significant baroclinic instabilities (PCr) are also associated with the wavetrain most notably in the polar jet between 0°E and 120°E during the summer and with the establishment of the subtropical jet between 60°E and 240°E in the austral winter. Anomalous baroclinic instabilities (PCr') are coincident with $PV'_{320\text{K}}$ anomalies and have dipolar structures in the meridional direction. In the summertime, $RWS'_{300\text{hPa}}$

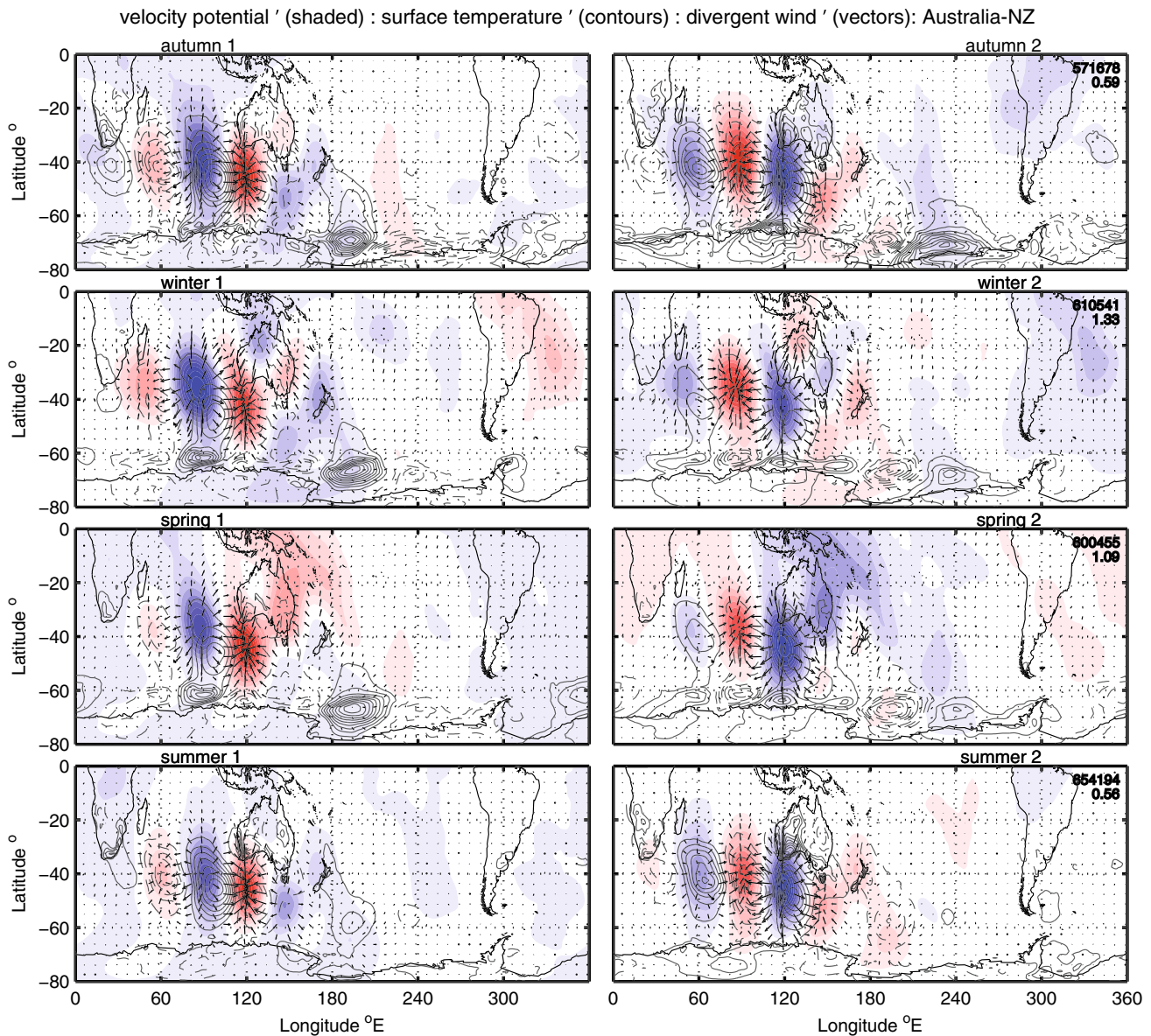


Fig. 7 As for Fig. 5 but for $\chi'_{300\text{hPa}}$ (shaded), SAT' (contours) and $\mathbf{v}'_{\chi'_{300\text{hPa}}}$ (vectors)

and PCr' anomalies are located entirely within the polar jet, but in the wintertime, they project into the subtropical jet and in particular into the Tasman Sea region.

Warm summertime SAT' anomalies are clearly associated with negative $\chi'_{300\text{hPa}}$ anomalies and divergent anomalous winds $\mathbf{v}'_{\chi'_{300\text{hPa}}}$ vectors, indicating regions of enhanced and persistent convection (Fig. 7) and anticyclonic (cyclonic) Rossby wave source regions (Fig. 6). In the winter and spring $\chi'_{300\text{hPa}}$ anomalies, there is some suggestion that tropical-extra tropical interactions may be at play, however these interactions are very weak and there is little evidence to support strong coupling between the tropics and midlatitudes in the other diagnostics. A more likely explanation is that disturbances (baroclinic instability) localised within the

subtropical jet are driving anomalous $\chi'_{300\text{hPa}}$ during these periods.

4.3 Indian sector

We now move our attention westward to the Indian sector between 120°E to 0° . In Fig. 8 we superimpose FEM-BV-VARX composite PCr' anomalies onto the $u_{300\text{hPa}}$ winds. We see baroclinic instabilities during the summer and autumn, localised about the midlatitude jet between 120°E and 300°E . In the winter and spring, there is a noticeable broadening of the meridional extent of PCr' anomalies from the Antarctic continent to Madagascar as the subtropical jet establishes and then decays. In the springtime in particular a well defined

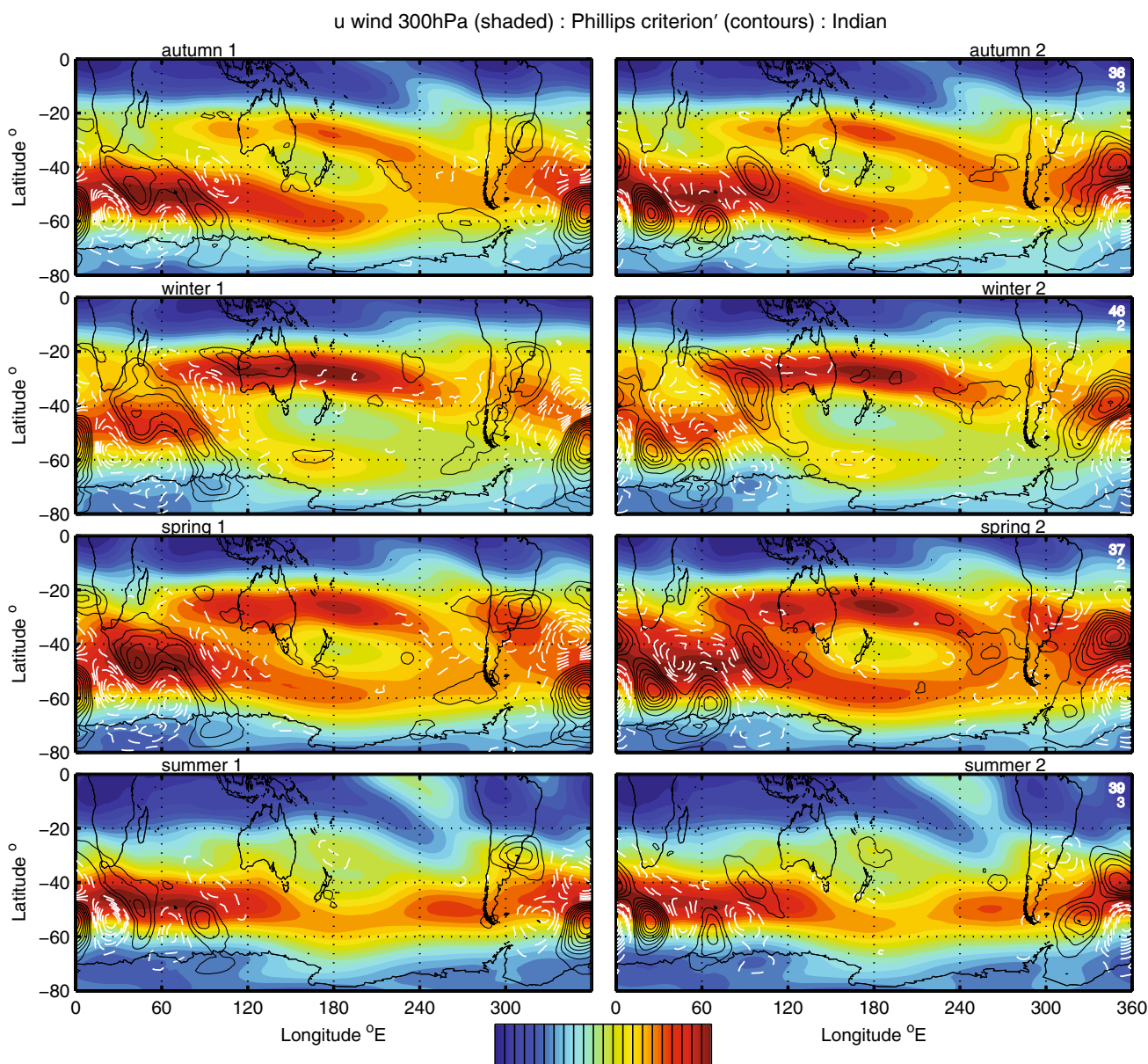


Fig. 8 Composite FEM-BV-VARX states for the Indian sector. $u_{300\text{hPa}}$ (shaded) and PCr' (black-positive, white-negative: contours). The color bar for the full $u_{300\text{hPa}}$ field is at the bottom of the figure

split jet occurs and, in both the winter and spring, PCr' anomalies are seen to extend well into the subtropics and over the Australian mainland. $RWS'_{300\text{hPa}}$ and $\psi'_{500\text{hPa}}^{\text{eddy}}$ anomalies (Fig. 9) span the Atlantic and Indian oceans. Whereas $RWS'_{300\text{hPa}}$ anomalies form a regular wavetrain, $\psi'_{500\text{hPa}}^{\text{eddy}}$ anomalies exhibit a large double-lobed anomaly between 30°E and 80°E , also evident in anomalous $PV'_{320\text{K}}$, $Z'_{g500\text{hPa}}$ and $\psi'_{500\text{hPa}}$ (not shown). In the winter, $RWS'_{300\text{hPa}}$ anomalies become meridionally-elongated before contracting in the winter, consistent with PCr' anomalies.

Warm SAT' anomalies are again clearly associated with negative $\chi'_{300\text{hPa}}$ anomalies and divergent wind $\mathbf{v}'_{\chi'_{300\text{hPa}}}$

vectors, indicating regions of enhanced and persistent convection (Fig. 10). The summertime $\chi'_{300\text{hPa}}$ wave train extends from South America to the Western Australian coast and has maximum magnitude upstream of Cape Town between 330°E and 360°E . The wintertime circulation becomes significantly more complex, with the wavetrain nodes becoming elongated as the subtropical jet forms. In the summer, SAT' anomalies are completely located where the $u_{300\text{hPa}}$ winds are strongest, but move poleward as the sea ice forms in the winter and large surface temperature gradients are manifest along the Antarctic Peninsula. There is again little evidence that tropical processes play a role in the dynamics of these persistent states.

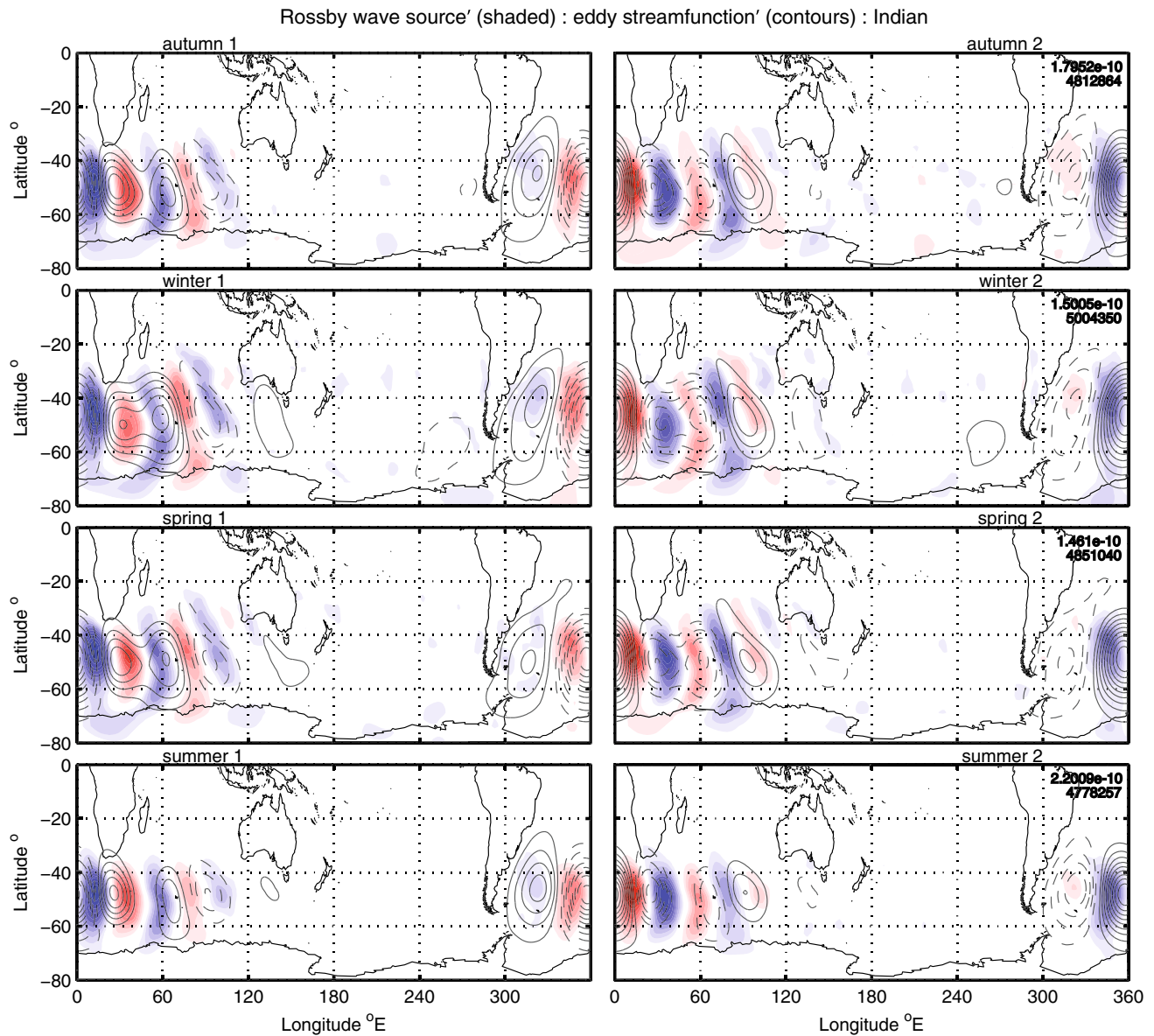


Fig. 9 As for Fig. 8 but for $RWS'_{300\text{hPa}}$ (shaded) and $\psi'_{500\text{hPa}}^{\text{eddy}}$ (contours)

4.4 South America sector

The South American sector spans 0° to 120° . In Fig. 11, $\psi'_{500\text{hPa}}$ and PCr' anomalies are superimposed onto the full field $\psi_{500\text{hPa}}$ contours. The anomalous $\psi'_{500\text{hPa}}$ streamfunction (also $\psi'_{500\text{hPa}}^{\text{eddy}}$ Fig. 14) shows equivalent structure to the wintertime PSA 1 pattern of Mo and Higgins (1998) (their Fig. 1), obtained as the leading EOF of the low pass filtered 200 hPa eddy streamfunction based on the NCEP reanalysis data. PSA 1 was found to be in quadrature with the PSA 2 (second EOF of the 200 hPa eddy streamfunction) pattern with each explaining about 5 % of the variance. As such they represent an eastward propagating oscillating

teleconnection mode. Rogers and van Loon (1982), and subsequently Mo and Paegle (2001), found similar wave 3 standing wave structures in analyses of 500 hPa.

FEM-BV-VARX composite states represent here the quasi-stationary regimes associated with the combined PSA modes. Apart from the summertime, large localised baroclinic disturbances (PCr') are shown to occur between 20°S and 40°S in the composites. The contours of the full field $\psi_{500\text{hPa}}$ give some indication of the width of the mid-latitude circulation and the extent of the summertime contraction. PCr' anomalies tend to form dipolar structures in the meridional direction, which are coincident with the wavetrain and are largest in the wintertime. They are

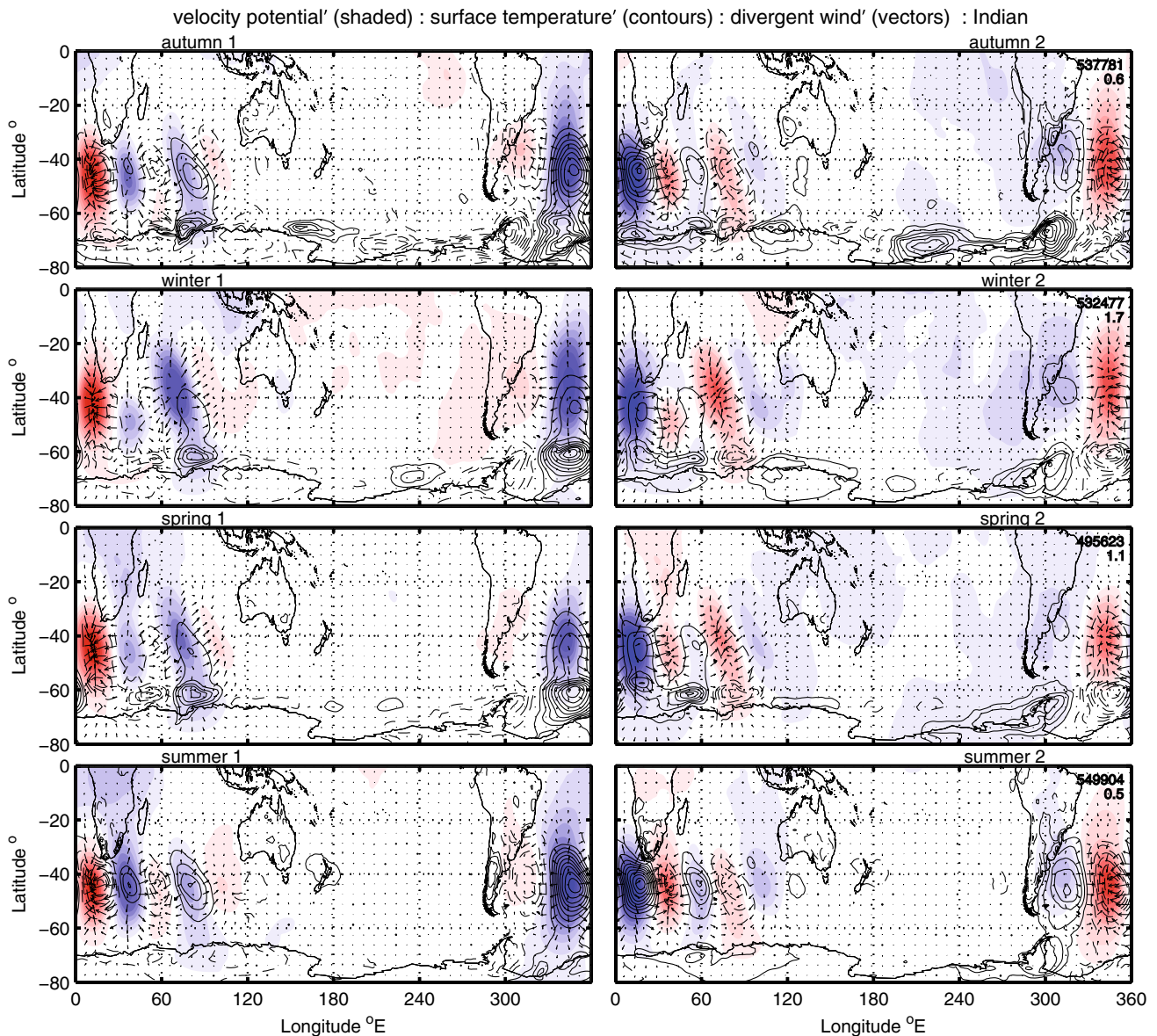


Fig. 10 As for Fig. 8 but for $\chi'_{300\text{hPa}}$ (shaded), SAT' (contours) and $\mathbf{v}'_{\chi'_{300\text{hPa}}}$ (vectors)

also highly correlated with the anomalous $u'_{300\text{hPa}}$ winds in Fig. 12. We also see that SAT' anomalies are anticorrelated with $\psi'_{500\text{hPa}}$ anomalies and positively correlated with anomalous $PV'_{320\text{K}}$ and $Z'_{g500\text{hPa}}$. In the winter, large SAT' anomalies extend equatorward from the Antarctic coastline to about 30°S with maxima at about 70°S . In the summer, the maxima move equatorward to between 50°S and 60°S as the jet contracts.

In Figs. 12 and 13 rising air and enhanced convection (negative anomalous $\chi'_{300\text{hPa}}$ and divergent $\mathbf{v}'_{\chi'_{300\text{hPa}}}$ vectors) are associated with warm SAT' and anticyclonic $RWS'_{300\text{hPa}}$ anomalies occurring in quadrature with $\psi'_{500\text{hPa}}$ anomalies (Fig. 14). Contours of the full field $RWS_{300\text{hPa}}$ superimposed onto $\psi'_{500\text{hPa}}$ anomalies

show significant Rossby wave sources being generated about the Andes during the winter, and to a lesser extent, spring. In the summer and autumn, the subtropical jet collapses and all $RWS_{300\text{hPa}}$ activity moves poleward where meridional temperature gradients rather than topography become the major means by which waves are generated.

4.5 Pacific sector

The final sector, is the Pacific, spanning 60°W to 150°E . In this sector, the wintertime subtropical jet is fully resolved as evident in the wave 4–5 $PV'_{320\text{K}}$ anomalies shown in Fig. 15. The subtropical and polar jets are clearly defined by the $u_{300\text{hPa}}$ wind contours. Wintertime baroclinic

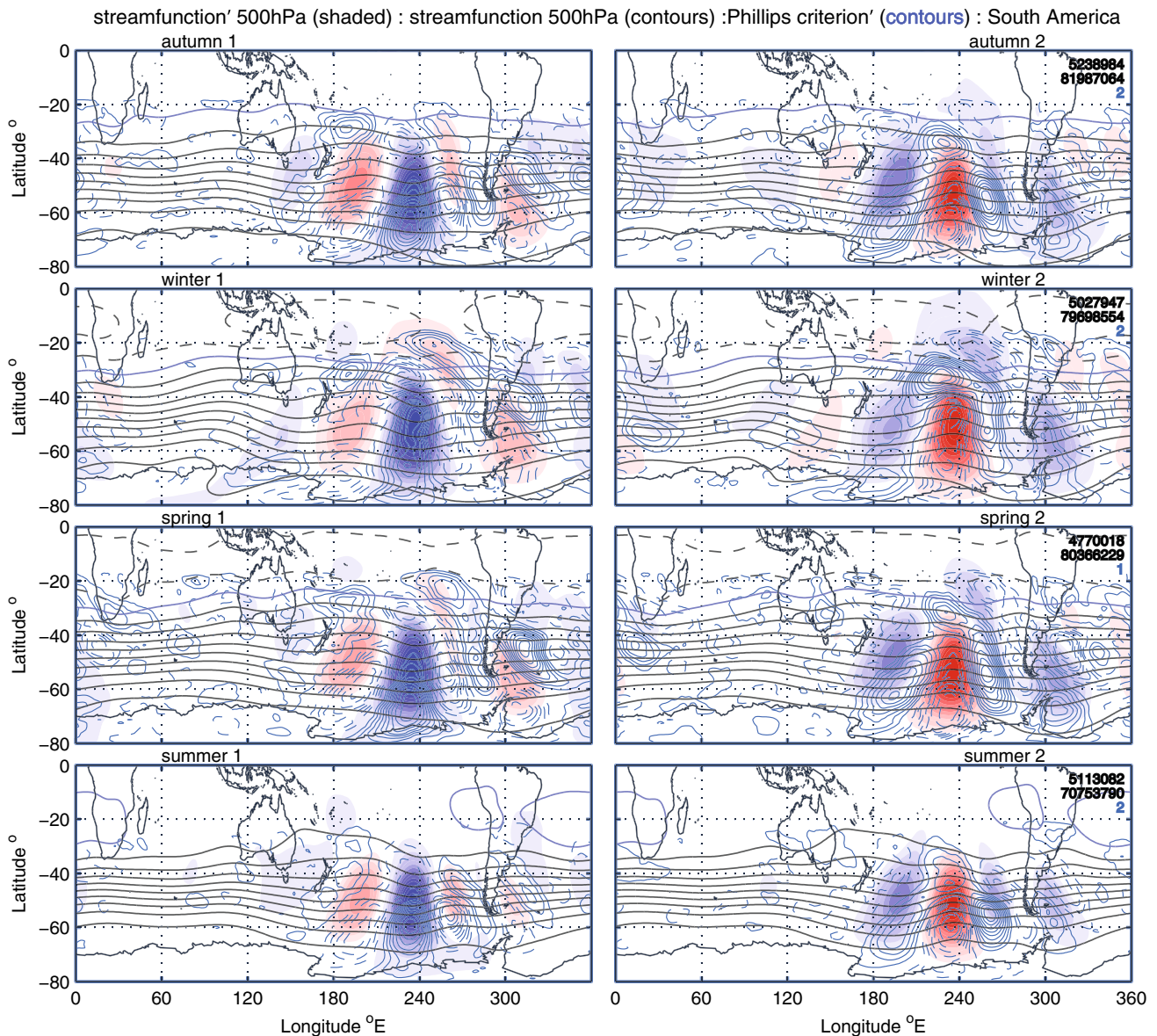


Fig. 11 Composite FEM-BV-VARX states for the South American sector. $\psi'_{500\text{hPa}}$ shaded, $\psi_{500\text{hPa}}$ (contours) and PCr' (blue contours)

instabilities are largely positively-correlated with $PV'_{320\text{K}}$ anomalies in both jets—with the exception of a very large $PV'_{320\text{K}}$ anomaly located around 150°E , 50°S , where the midlatitude jet splits. In this location, PCr' anomalies form a positive–negative (negative–positive) dipole in the meridional direction equatorward of 70°S about the positive (negative) $PV'_{320\text{K}}$ anomaly. As the circulation transitions through spring, anticyclonic (cyclonic) $PV'_{320\text{K}}$ anomalies in both jets merge, forming the wavetrain confined within the summertime polar jet. The reverse occurs in the autumn as summer transitions to winter.

Anomalous SAT' (Fig. 16) appears upstream of and in quadrature with $Z'_{g500\text{hPa}}$ anomalies, and with greatest

meridional extent in the spring and autumn. In the winter, SAT' anomalies are largely poleward of 60°S , apart from the region 120°E to 180°E where they extend into the interior of the Australian mainland. In the summertime, positive (negative) SAT' anomalies are at their most intense over the southeastern states of Australia, in particular South Australia, Victoria and Tasmania. The positive (negative) summertime $Z'_{g500\text{hPa}}$ anomalies coincide with strong blocking (zonal) flows and positive (negative) SAT' anomalies. The anti-cyclonic $Z'_{g500\text{hPa}}$ anomalies shown in Fig. 16 are an indication of persistent blocking, which when combined with the large positive SAT' anomalies can be further associated with anomalously warm temperatures

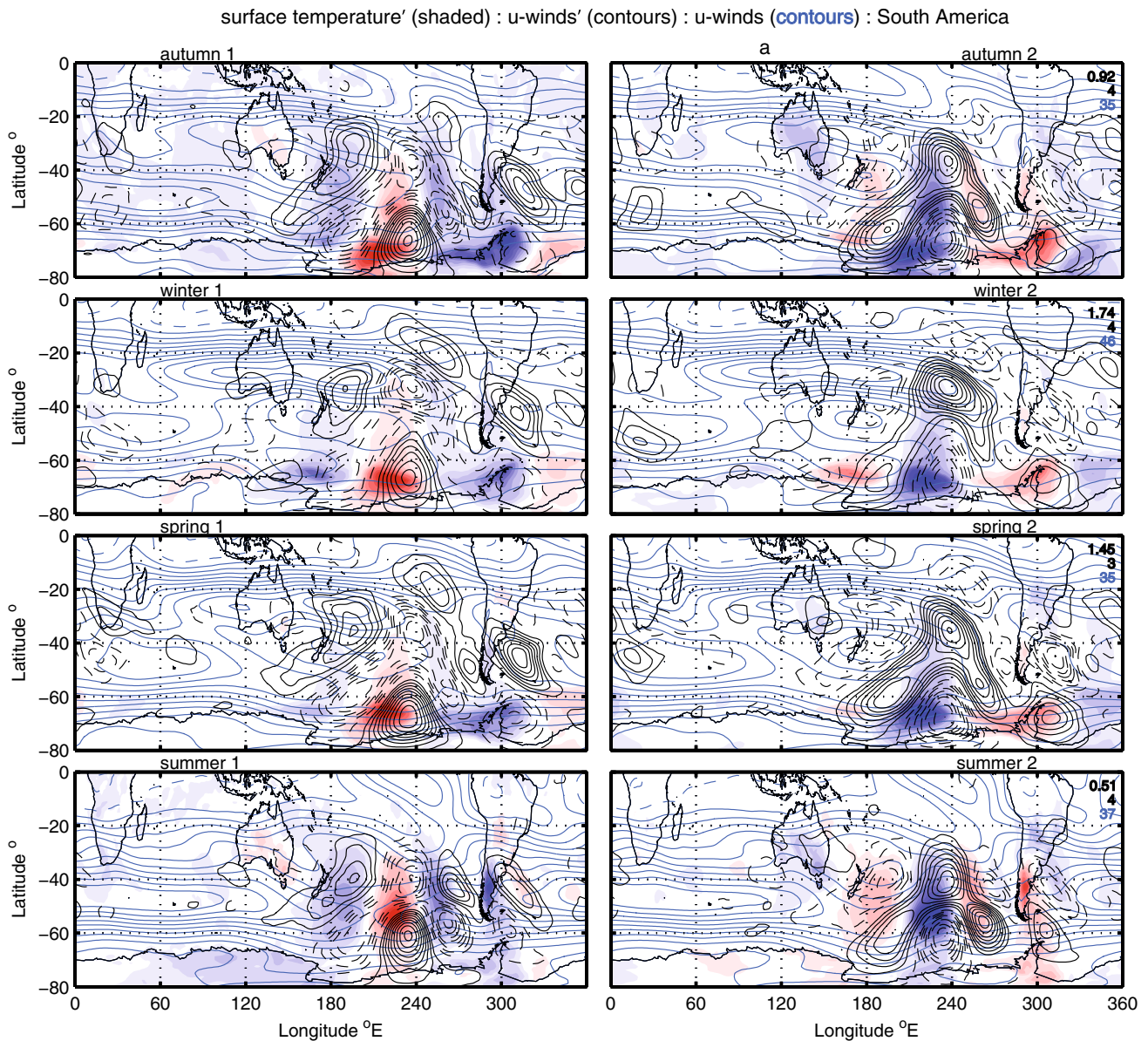


Fig. 12 As for Fig. 11 but for SAT' (shaded), $u'_{300\text{hPa}}$ (contours) and $u_{300\text{hPa}}$ (blue contours)

over Melbourne. Interestingly the $Z'_{g500\text{hPa}}$ wave structures are consistent with recent composite patterns of $Z'_{g500\text{hPa}}$ for heat wave events over Melbourne as described by Pezza et al. (2012) (see their Fig. 6b) however, a separate study is clearly required to explicitly separate extremes from more generally warm events.

As in the other sectors, regions of rising (descending) air and upper level divergence (convergence) are coincident with anti-cyclonic (cyclonic) $RWS'_{300\text{hPa}}$ (Fig. 17) and warm (cool) SAT' anomalies. Positive (negative) $PV'_{320\text{K}}$ anomalies are centred about large positive–negative (negative–positive) longitudinal horizontal gradients in anomalous $\chi'_{300\text{hPa}}$. The Tasman Sea region clearly defines the

branching of the midlatitude jet for the anomalous winter-time circulation.

4.6 Secular trends in Z_{g500} regimes

In this section, we examine secular trends in the Z_{g500} cluster states for the hemisphere and all sectors. In all cases, the FEM-BV-VARX analysis of the JRA55 reanalysis reveals two significant metastable states. In order to examine inter-annual variability we calculate the percentage of time resident in a given state for each year of the reanalysis period and then apply a LOESS fit to the time-averaged data.

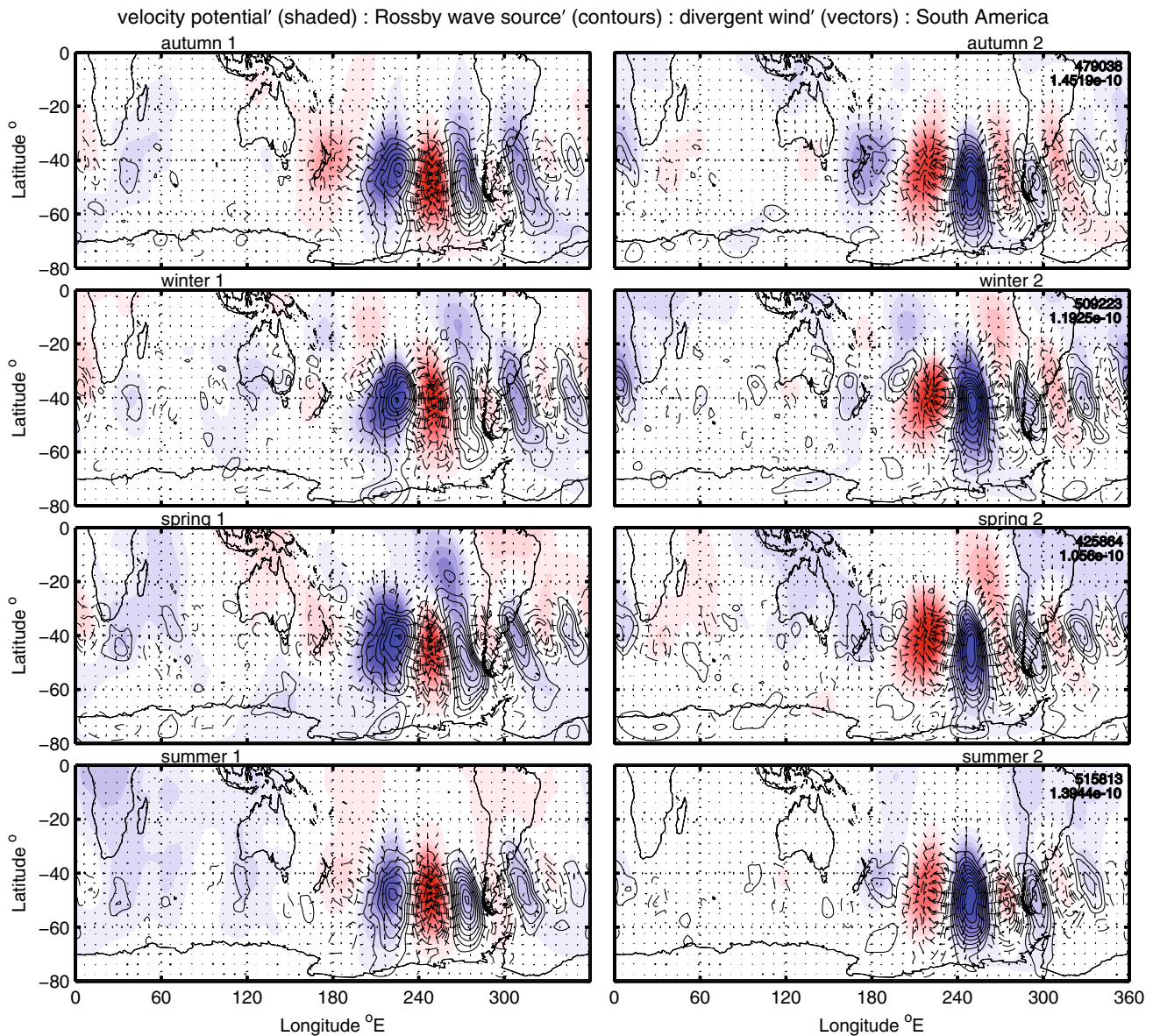


Fig. 13 As for Fig. 11 but for $\chi'_{300\text{hPa}}$ (shaded), $RWS'_{300\text{hPa}}$ (contours) and $v'_{\chi_{300\text{hPa}}}$ (vectors)

4.6.1 Southern Hemisphere

For the SH, the geographical structure of the two annual regimes (Fig. 3) show a distinct wave 3 (polar jet)–wave 5 (subtropical jet) pattern, where state 2 has the opposite polarity to state 1. The summer and winter secular trends (Fig. 18) show that state 2 dominated the tropospheric circulation prior to 1980 after which state 1 became generally preferred. This shift in regimes is also reflected in the annual secular trend. Referring to Fig. 3b, we see that this hemispheric regime transition of the late 1970s–early 1980s corresponds to stronger zonal flows in the region to the south of the Australian mainland (i.e. negative $PV'_{320\text{K}}$ and Z'_{g500}) and a general reduction in baroclinic instability in the

subtropics between 90°E and 180°E (Fig. 3c). To the South, again between 90°E and 180°E, the anomalously-divergent winds and $RWS'_{300\text{hPa}}$ (Fig. 3d) are generally largest poleward of 50°S. Over the western Indian Ocean, the transition to state 1 post 1980 corresponds to a significant reduction in baroclinic instability and more convergent upper level winds. The same is true for the eastern Atlantic region to the east of South America.

The relative frequency and duration of events is shown in the histogram (Fig. 19) where, as in the study of O’Kane et al. (2013) we first take a 5-days running average of the posterior model affiliation sequence, then we further define a transition state according to the following: an anomaly at any particular time will be assigned to the transition state

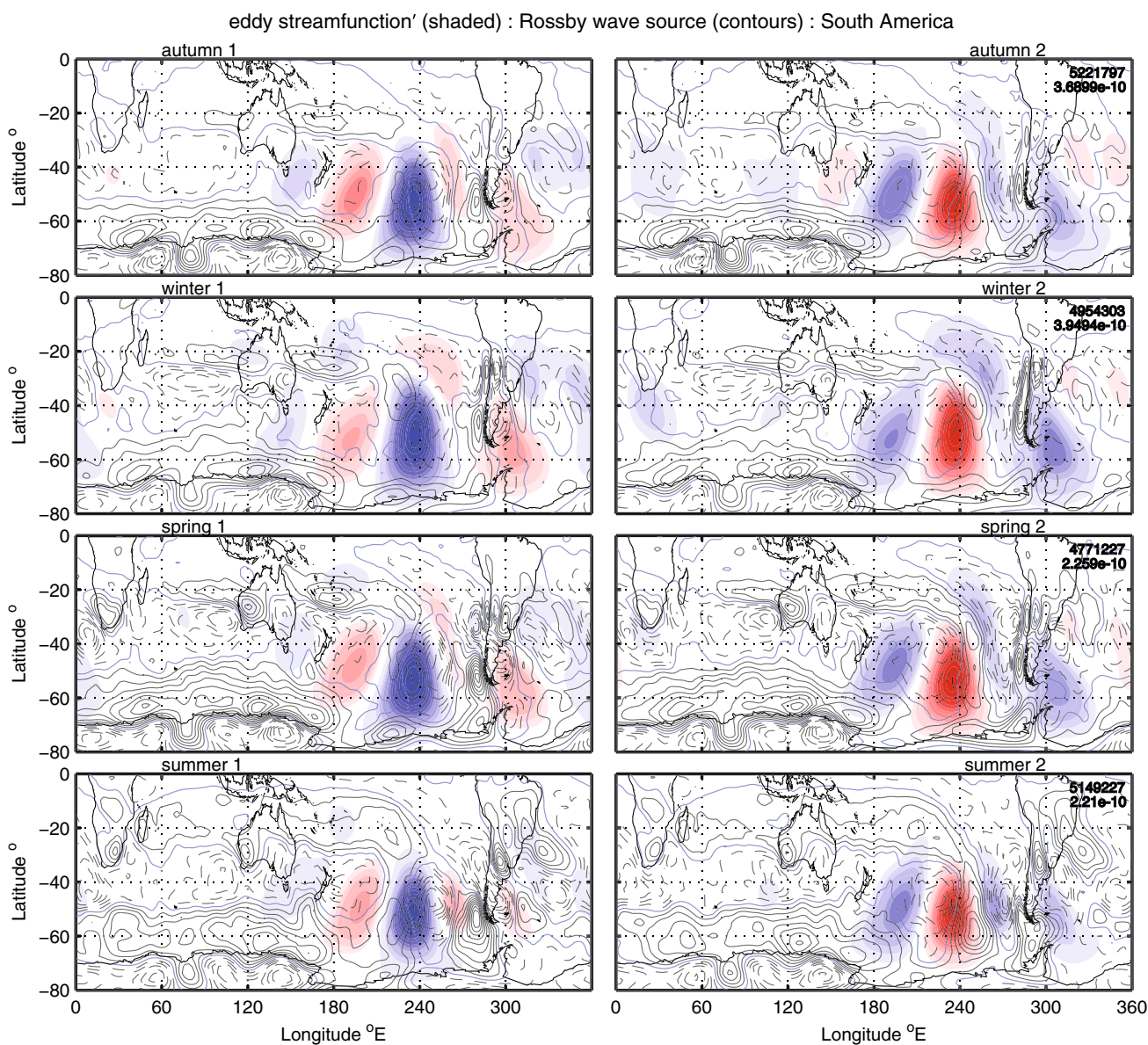


Fig. 14 As for Fig. 11 but for $\psi'_{500\text{hPa}}^{\text{eddy}}$ (shaded) and $RWS_{300\text{hPa}}$ (contours)

if for any given 5-days period the posterior model affiliation sequence (Viterbi path) occupies no more than 3 days in any given state. The transition state is applied to cleanly separate the metastable states according to their persistence and is analogous to that applied by Tibaldi et al. (1994) to blocking. The histogram shows that both regimes favour about 4–5 days in their persistence, with relatively infrequent events of 8–10 days duration. Although the secular trend is towards state 1, when the entire period is taken into account both states occur with similar frequency. The transition state histogram indicates more than 50 events where no persistent state occurred during periods of 30 days or more.

4.6.2 Australian–NZ sector

In the Australian–NZ sector (Fig. 20), we note that the summer (winter) periods are dominated by state 1 (state 2) respectively. In the summer state 1, SAT' anomalies (Fig. 7) are maximum in the polar jet with a large warm anomaly at 100°E, associated with positive $PV'_{320\text{K}}$, anticyclonic $Z'_{500\text{hPa}}$ anomalies (Fig. 6) and upper level divergence. In this season, significant anomalous SAT' is also manifest on the coast of Western Australia about Perth, suggesting that anomalously warm periods in the major Western Australian population centre are strongly dependent on the formation of persistent anticyclones in this node of the circumpolar

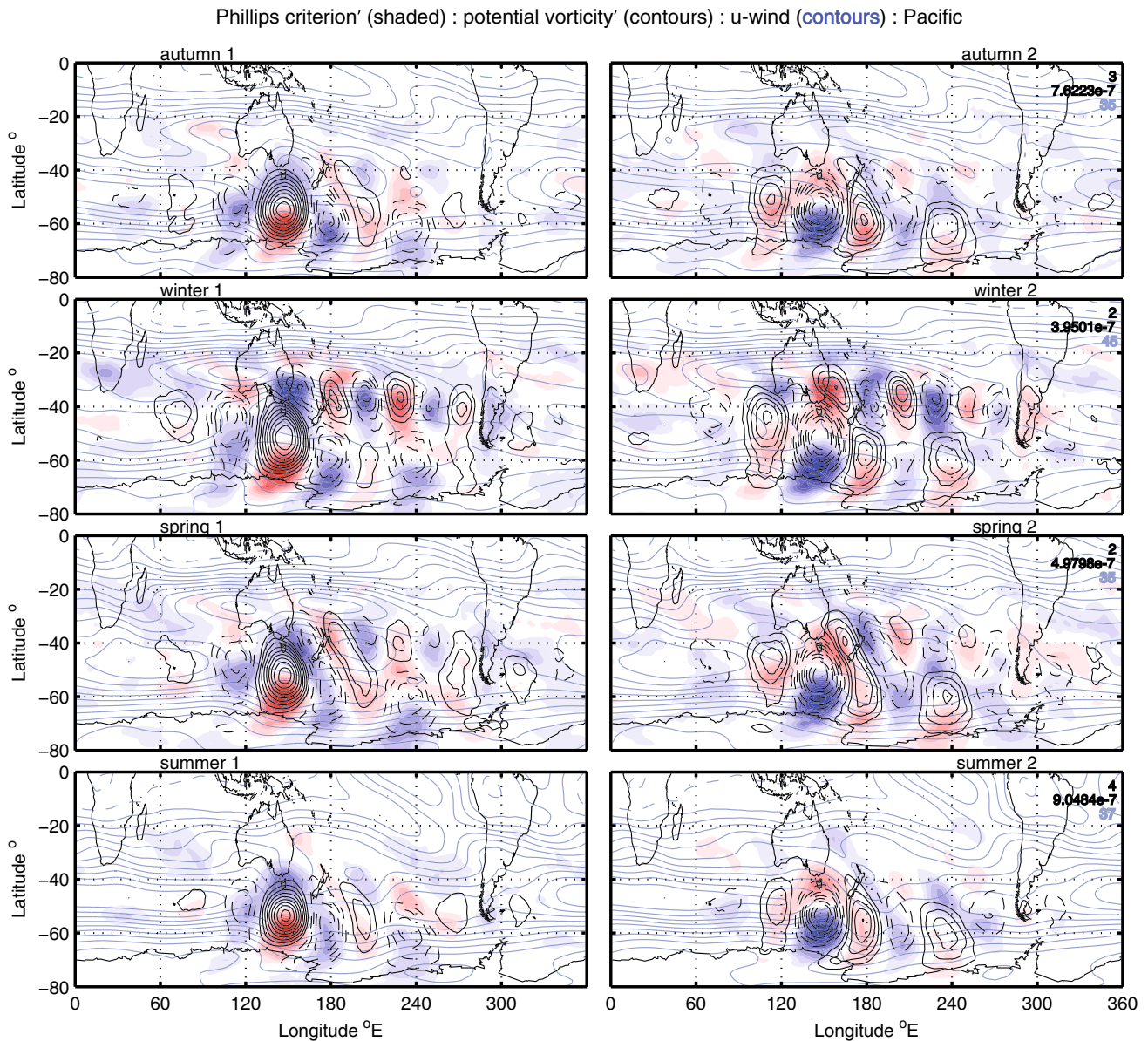


Fig. 15 Composite FEM-BV-VARX states for the Pacific sector. PCr' , PV'_{320K} (contours) u_{300hPa} (blue contours)

waveguide. For the summer, state 1 baroclinic instabilities are significant at 55°S between 100°E and 120°E just poleward of the large warm SAT' anomaly. From Fig. 20, we see that the wintertime circulation largely favours state 2. The preferred wintertime state is characterised by warm SAT' anomalies to the south of Perth and to the southeast of Madagascar (Fig. 7). Upper level divergence (Fig. 7), strong baroclinic instabilities and the generation of Rossby waves (Fig. 6) are also evident at this location for the winter. Prior to 1980, there is a noticeable negative trend in the summertime state 1, which is reversed post 1980. The wintertime secular trend shows marked decadal variations of between 10 and 20 years, but no clearly discernible

trend overall. The annual variations appear to be largely dominated by the wintertime circulation. On average states tended to persist for about 4–5 days although there were found a very few events that persist out to 20 days.

4.6.3 Indian sector

Secular trends in the Indian sector are characterised by significant decadal variations (Fig. 21). In particular, the transition seasons autumn and spring and the winter show a preference for state 2 post 1980 until the late 2000s. Both transition seasons show that, prior to 1980, they were in state 1 for more than 50 % of the time. The summer

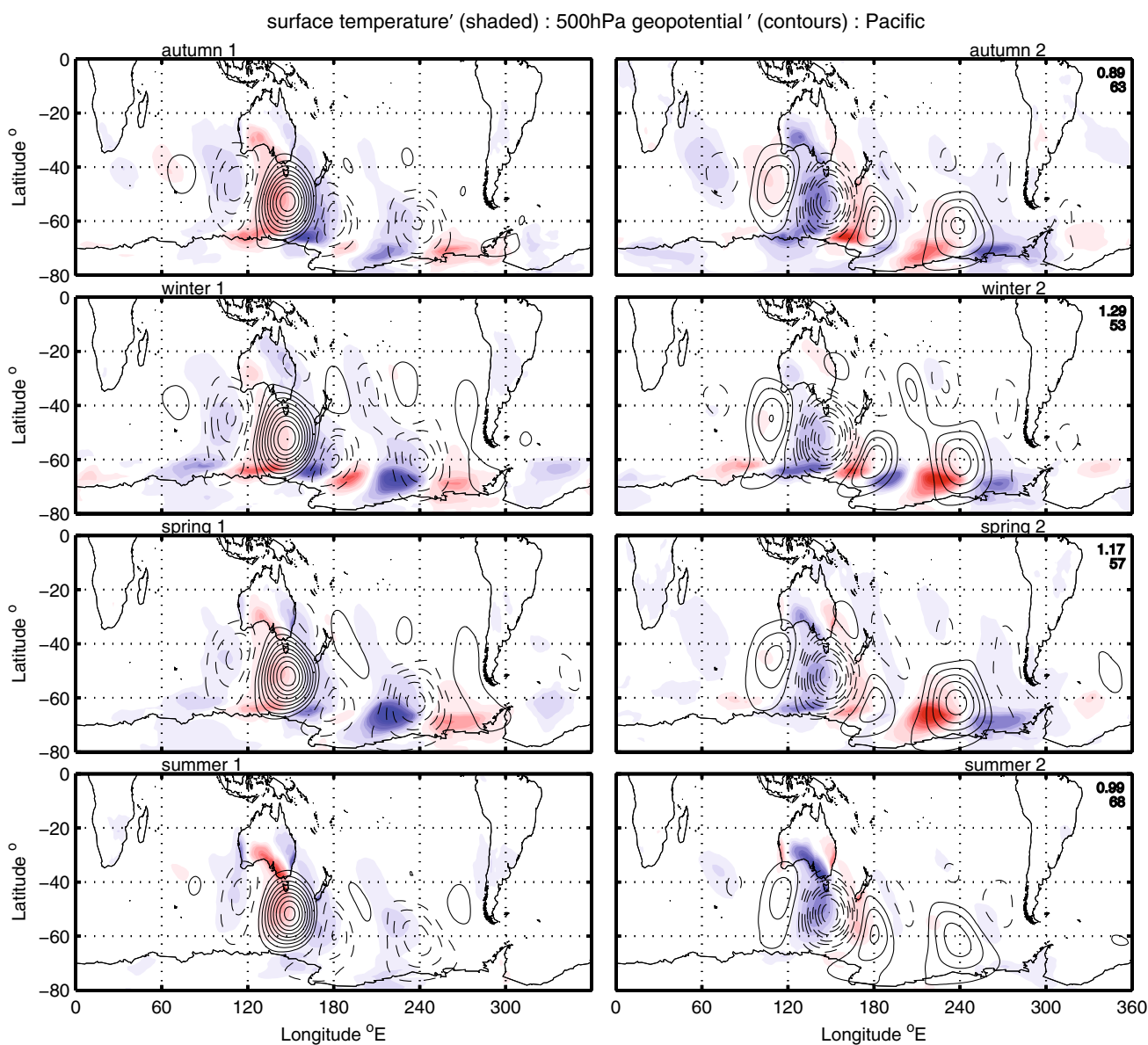


Fig. 16 As for Fig. 15 but for SAT' (shaded) and $Z'_{g500hPa}$ (contours)

favours state 1 during the periods 1958–1970 and from 1995 to present, with no clear preferred state in the interim period. The trend in annual residence percent shows a general preference for state 2 post 1980. State 2 is characterised by a wave 3–4 pattern with a large anticyclone located upstream of Cape Town (Fig. 9). Baroclinic disturbances associated with state 2 do not extend into the subtropical jet during the winter as compared to those of state 1 (Fig. 8). Summertime state 1 baroclinic disturbances are well poleward relative to those of state 2 with the most significant convective anomaly (Fig. 10) occurring at the node centred at 345°E. As with the Australian–NZ sector, states tended to persist for 4–5 days with no persistent events occurring beyond 15 days duration.

4.6.4 South American sector

The South American sector secular trends in residence percentage (Fig. 22) are complex, displaying large multi-year to decadal variations and also periods of relative quiescence. The largest variations occur for the autumn and winter. In the winter, state 2 was preferred between about 1965–1975, state 1 from 1975 to 1990 and state 2 from 1990 to 2007. The autumn shows large variations from about 1985 to the early 2000s, shifting between state 1 (1985–1995) and state 2 (1995–2003). There are no clear trends in the summer, although there does seem to be some preference for state 1 between 1985 and 2003 and state 2 thereafter. As with the other sectors, most of

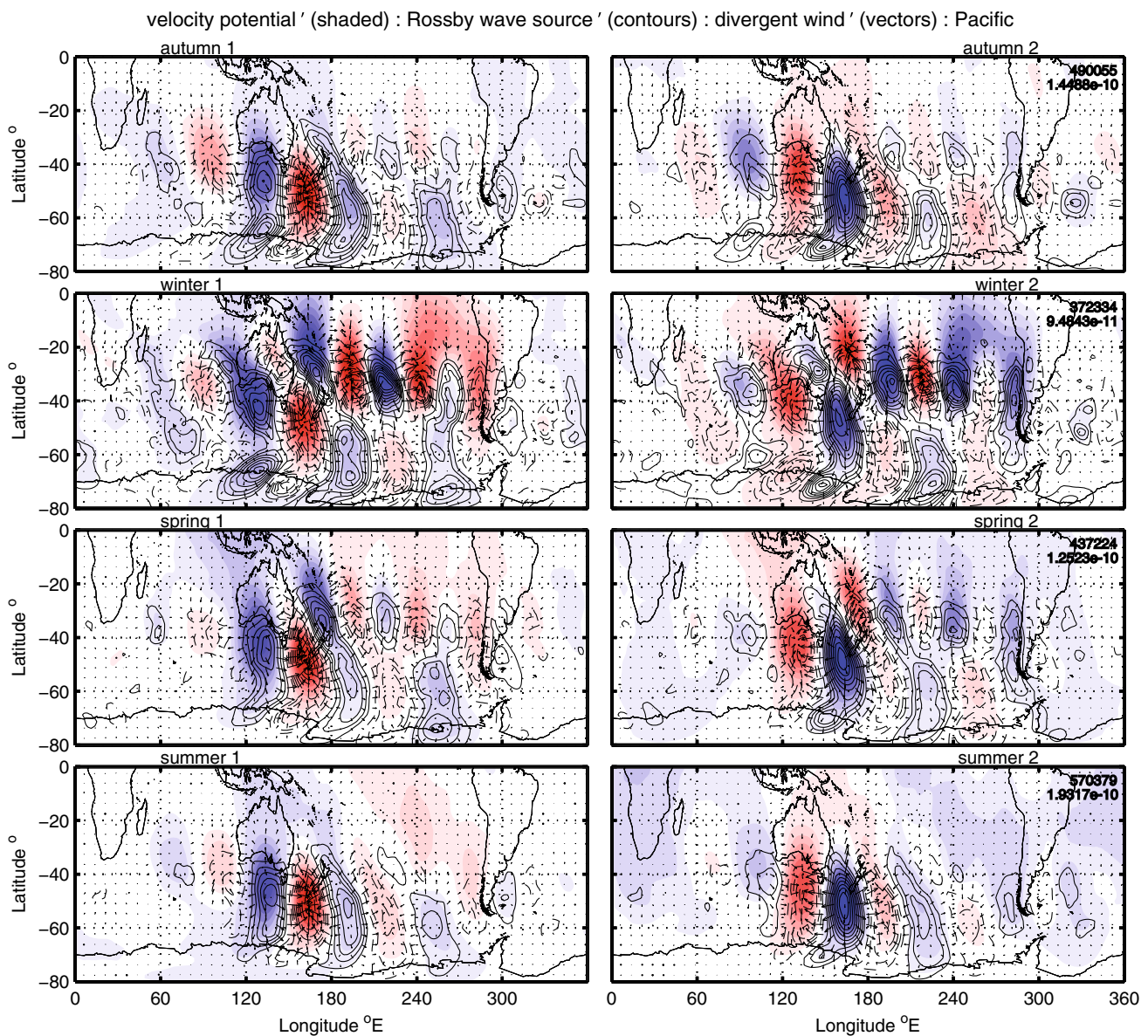


Fig. 17 As for Fig. 15 but for $\chi'_{300\text{hPa}}$ (shaded), $RWS'_{300\text{hPa}}$ (contours) and $v'_{\chi'_{300\text{hPa}}}$ (vectors)

the individual events persist for between 4 and 5 days with exceptional events persisting for up to 14 days.

4.6.5 Pacific sector

As for the full hemisphere, in the Pacific (Fig. 23) the summertime residence percentage shows a distinct transition from a period of relatively regular decadal variations between states to one in which it is locked into a dominant state 1 post 1980. The transition seasons show similar shifts between the respective regimes about every 5–10 years. The winter has a slight preference for state 2 prior to 1980, after which only the period 1996–2002 shows a marked transition to state 1. The summertime state 1 is characterised by a significant anticyclonic

500 hPa height anomaly to the South of the Tasman Sea (Fig. 16). This pattern is associated with anomalously warm surface air temperatures from Tasmania extending to Victoria then inland and along the coast to the southwest, and is further associated with reduced baroclinic instability between the Australian mainland and 50°S (Fig. 15). The wintertime circulation is dominated by the subtropical jet with state 1 (state 2), displaying convergent (divergent) winds in the Tasman Sea and reduced (enhanced) convection in the subtropical South East Pacific (Fig. 17). The annual residence percentage favours state 1 post 1980, indicating that the summertime circulation trends are dominant. Again, most individual events persist for between 4 and 5 days with exceptional events persisting for up to 16 days (Fig. 23).

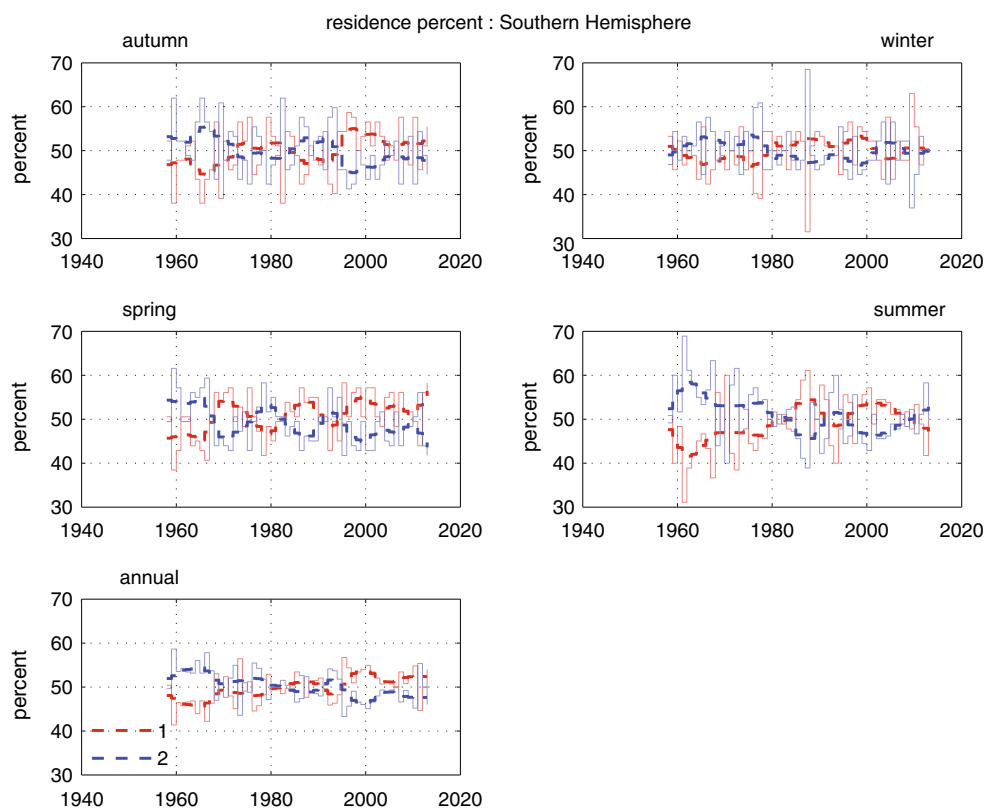


Fig. 18 Percentage of time resident in state 1 (red) or state 2 (blue) calculated from FEM-BV-VARX model affiliation sequence determined from JRA55 500-hPa reanalysed geopotential height and after a 5-days running average for each of the seasons and the annual

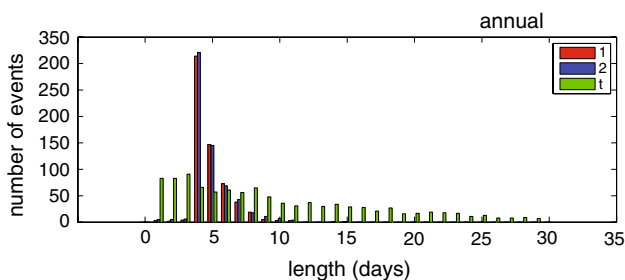


Fig. 19 Histogram of the number of events of a given duration corresponding to state 1 (red) and state 2 (blue) and a transition state (green) calculated over the entire reanalysis period for the SH. An anomaly at any particular time is assigned to the transition state if for any given 5-days period the model affiliation sequence (Viterbi path) occupies no more than 3 days in any given state. Transition events of 30 days or more are few and not shown

5 Summary and conclusions

We have applied, for the first time, an advanced nonstationary timeseries analysis method to a high resolution atmospheric reanalysis in order to identify persistent quasi-stationary states that form in the waveguides of the SH. Specifically,

period has been applied. The dashed lines are a LOESS fit to the time-averaged data. The solid lines are the values and averaging periods of the data

we were able to resolve disturbances located in the subtropics and midlatitudes and confined within the jets which act as waveguides. Our results are consistent with earlier studies, such as the one by Ambrizzi et al. (1995), which characterise these waveguides as having a wave 3–wave 5 structure, as source regions from which stationary Rossby waves emanate (Freitas and Ambrizzi 2012; Ding et al. 2012), and where significant systematic changes in baroclinic instability and storm formation over recent decades have occurred (Frederiksen et al. 2011). In considering a comprehensive set of diagnostics, we have shown the equivalence of $\psi_{500\text{ hPa}}$, $\psi_{500\text{ hPa}}^{eddy}$, $Z_{g500\text{ hPa}}$ and $PV_{320\text{ K}}$ as indicators of persistent anomalies both for the hemisphere and when considering regional teleconnection (blocking) patterns. In this regard, no single diagnostic—whether on isentropes or isobars—was found to be of more utility than the other—in this respect our results are consistent with those of Barnes et al. (2012) who showed that seasonal blocking climatologies are very similar between indices in terms of $Z_{g500\text{ hPa}}$ and $u_{500\text{ hPa}}$ fields and the $2PVU$ (θ_2) surface when the same blocking regime method is applied. Regardless of sector, we found that persistent anomalies in height or potential vorticity formed preferentially on the nodes of the circumpolar waveguide.

Fig. 20 As for Fig. 18 but for the Australian–NZ sector

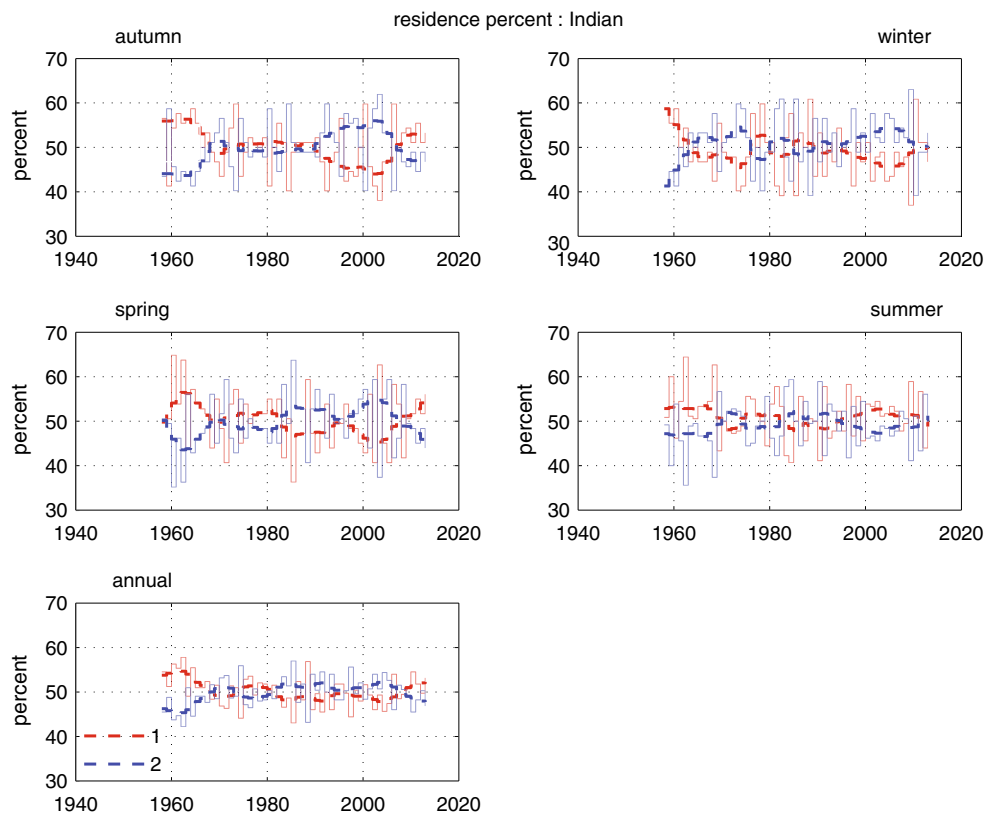
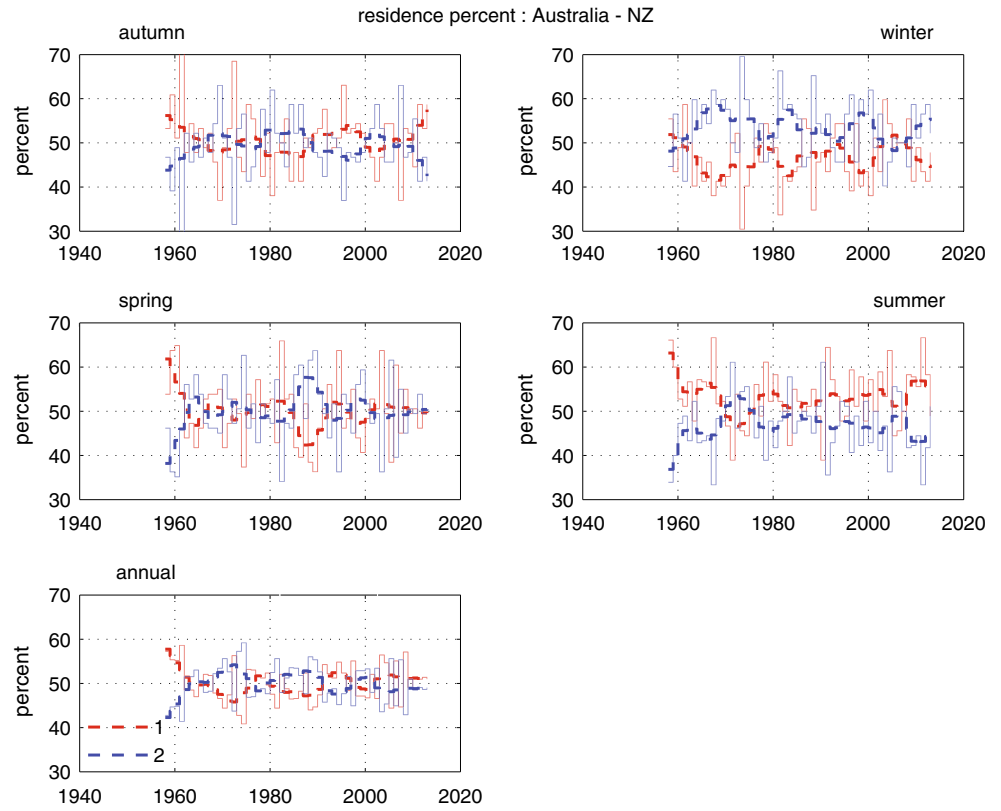


Fig. 21 As for Fig. 18 but for the Indian sector

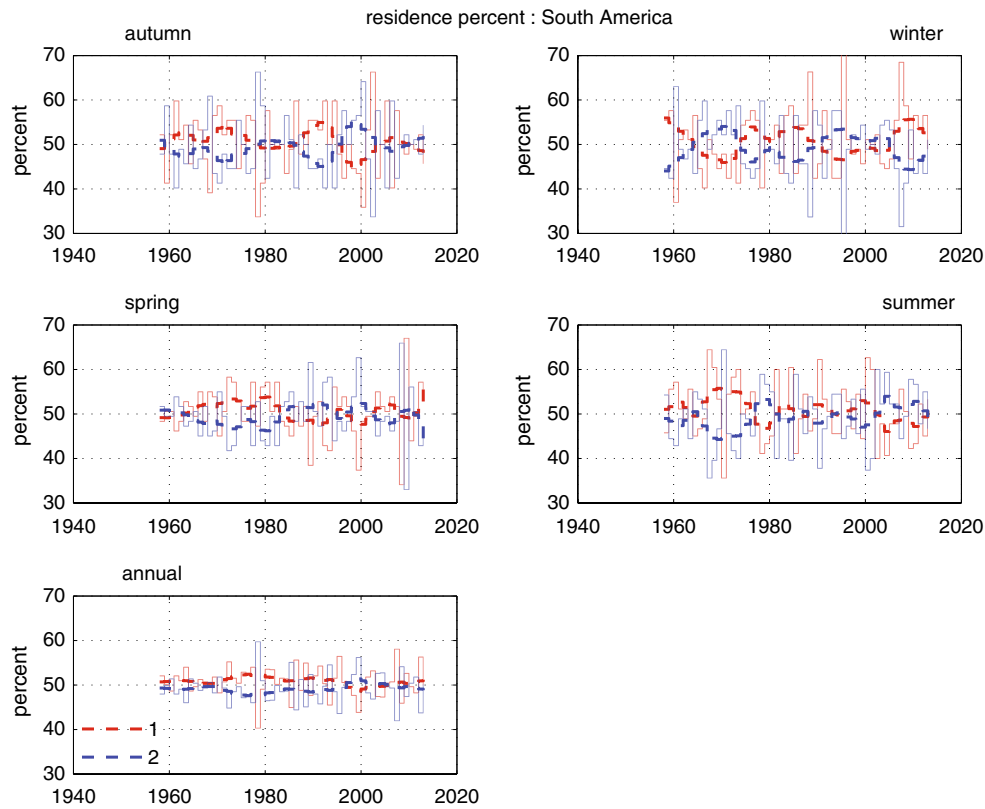


Fig. 22 As for Fig. 18 but for the South American sector

In general, warm anomalous SAT' was highly correlated with negative (positive) $\chi'_{300\text{hPa}}$, divergent (convergent) $\mathbf{v}'_{\chi'_{300\text{hPa}}}$ and positive (negative) $RWS'_{300\text{hPa}}$. Thus warm surface air temperatures initiate a rising air column, upper level divergence and anticyclonic Rossby wave source generating stationary Rossby waves. Similarly, cool surface air temperatures indicate subsidence, upper level convergence and cyclonic Rossby wave sources. To understand large scale convection patterns, we used velocity potential, a large scale diagnostic whose maximum values occur over the tropics where anomalously positive (negative) values are indicative of weak (deep) convection and reduced (enhanced) precipitation. In general we found $\chi'_{300\text{hPa}}$ anomalies occurred coincident with $RWS'_{300\text{hPa}}$.

On the synoptic timescales considered, we found little to indicate sustained localised Rossby wave sources in the tropics, rather we find all significant source regions occurring in either the subtropical Pacific or confined within the waveguides of the seasonally varying basic states. We find that baroclinic disturbances originating from both local and remote sources interacting with local stationary Rossby wave sources close to the nodes of the waveguide are the dominant mechanism in the formation of persistent synoptic features. We see little direct evidence of sustained remote stationary Rossby wave generation from the tropics

relevant to the SH midlatitudes on synoptic timescales. This is not to say that such processes do not occur but that they are transient and generally weak relative to the interactions that occur within the waveguide. Undoubtedly on larger spatio-temporal scales—for example on the intraseasonal scales of the MJO—the tropics are crucial (see for example Figure 10 of Frederiksen and Lin 2013). We point out that studies finding tropical sources of stationary Rossby waves either impose an anomalously large source via tropical SST anomalies (Li et al. 2015) or employ correlations and regressions to infer indirect forcing (Ding et al. 2012). In terms of underlying mathematical assumptions, FEM-BV-VARX is much more general and less restrictive than multi-linear regressions (Franzke et al. 2015) and causal in the sense of Granger (Gerber and Horenko 2014).³

In the South American sector, we found a PSA pattern consistent with that described by Ding et al. (2012), however we find that this PSA pattern arises from the combined effects of both a Rossby wave source in the

³ Here we specifically refer to Granger causality based on linear autoregressive models of the time series. From this perspective, the autoregressive time series model behind the FEM-BV-VARX is simply a non-stationary extension of the Granger-causality, with model coefficients being allowed to vary in time.

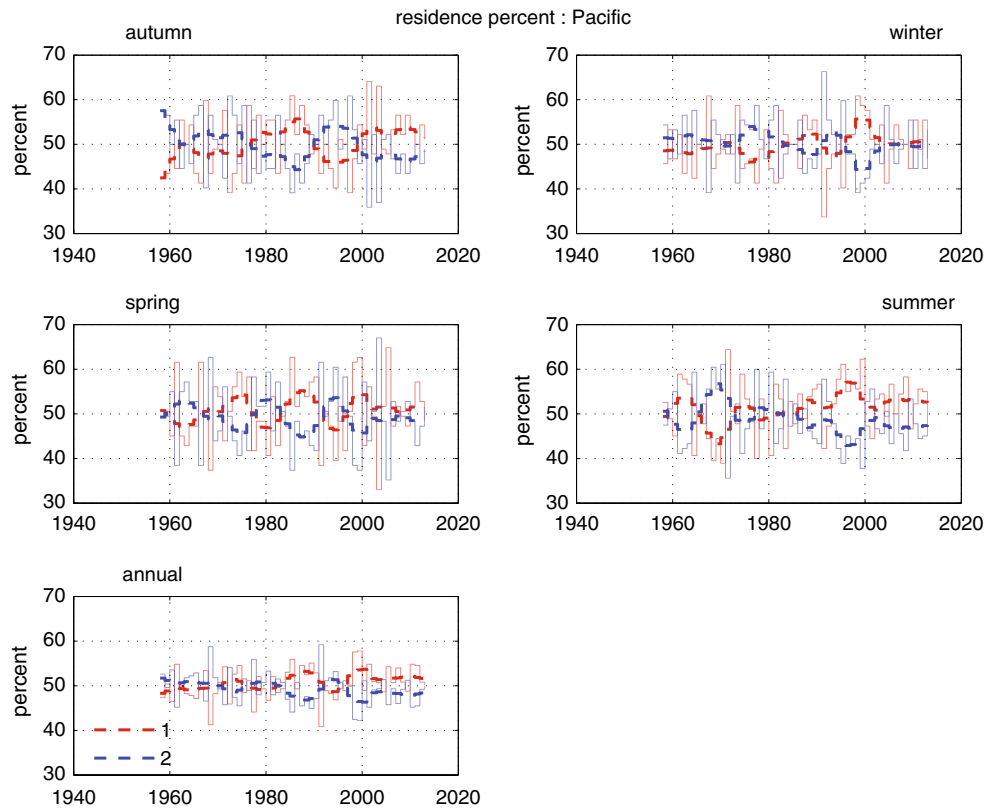


Fig. 23 As for Fig. 18 but for the Pacific sector

upper troposphere in the subtropics to the east of Australia and from upstream baroclinic instabilities generated in the Indian sector that amplify once entering either the subtropical or polar jet waveguides of the Pacific. Both kinds of disturbance are determined by the strength of the horizontal winds and by the sharpness of the meridional potential temperature gradients that set up the subtropical jet in the basic state flow. Again in agreement with Ding et al. (2012), we find the primary centre of action for the South American sector to be off the West Antarctic coast with poleward contraction in the summer and equatorward expansion in the winter, coincident with large Rossby wave sources in the wintertime subtropical jet. The primary difference between our study and that of Ding et al. (2012) is that we do not filter our data and are explicitly considering synoptic scale features. Further we do not find direct evidence for tropical (remote) sources for the PSA in either work.

In the Pacific, we identified the region where the wintertime subtropical and polar jets split between 130°E and 170°E to be a preferred location for the formation of very large positive geopotential height anomalies-blocks. Interestingly persistent positive $Z'_{g500\text{hPa}}$ and $PV'_{320\text{K}}$ anomalies in this sector were coincident with localised anomalously warm SAT' over the southeastern states of the Australian continent.

Variability over several years to decades was evident in all seasons and sectors as were secular trends apart from the South American sector. We summarise them thus

- *SH* A hemispheric regime transition occurred in the late 1970s–early 1980s corresponding to stronger zonal flows in the region to the south of the Australian mainland and a general reduction in baroclinic instability in the subtropics between 90°E and 180°E. Post 1980 over the western Indian Ocean and for the eastern Atlantic region to the east of South America, a significant reduction in baroclinic instability occurred coinciding with a shift to more convergent upper level winds.
- *Australian–NZ* The summer periods are dominated by significant surface air temperature anomalies over the coast of Western Australia about Perth as a result of persistent anticyclones in this node of the circumpolar waveguide. The preferred wintertime state is characterised by warm SAT' anomalies, upper level divergence, strong baroclinic instabilities and the generation of Rossby waves to the south of Perth and to the southeast of Madagascar. There occurred a noticeable regime shift in the summertime circulation about

1980 however, while the wintertime secular trend shows marked decadal variations of between 10 and 20 years, no clearly discernible trend is present.

- *Indian Post 1980*, the annual trend shows a general preference for a state characterised by a wave 3–4 pattern with a large anticyclone located upstream of Cape Town and where baroclinic disturbances are largely localised over the Southern parts of the Indian Ocean and do not extend into the subtropical jet during the winter—in contrast to the regime dominant in the earlier period where these disturbances extend across the Australian mainland.
- *South America* The South American sector secular trends display large multi-year to decadal variations but no clear trends with the largest variations occurring for the autumn and winter.
- *Pacific* The summertime trends exhibit a transition from a period of relatively regular decadal variations between states to the one characterised by a significant anticyclonic 500 hPa height anomaly to the South of the Tasman Sea, anomalously warm surface air temperatures extending from Tasmania to Victoria and then inland and reduced baroclinic instability between the Australian mainland and 50°S. The annual trend indicates that the summertime circulation trends are dominant.

We have shown the utility of an advanced clustering method to elicit the fundamental modes of the tropospheric circulation in high resolution reanalysis data. Our conclusions are based on a purely data-driven causality inference approach that has the potential to distinguish between simple correlations and the relevant underlying causation relations and has provided the clearest picture yet of the pivotal role of the jet stream waveguides in setting the fundamental modes of the troposphere. These modes provide a basis for understanding extremes, variation, and change in the atmosphere on short and long time scales.

In general we found that persistent coherent structures on synoptic spatio-temporal scales form on the nodes of the waveguides and are associated with local Rossby wave sources. The nodes of the waveguides determine, in large part, where resonant interactions are likely to occur e.g. between baroclinic instability and Rossby waves, and hence where persistent anomalies form. We also show anomalous Rossby wave source and potential vorticity, largely in quadrature, implying that Rossby waves breaking on positive height anomalies in the waveguide is a primary source of barotropic instability i.e. anomalous potential vorticity further acts to maintain the anticyclonic anomaly. Overall we find strong support for the instability paradigm i.e. that the flow is unstable to small local perturbations, and that there is little evidence that remote

Rossby wave sources from outside the waveguides play a significant role in the generation of persistent synoptic features.

The quasi-stationary states manifest in the waveguide exhibit variability on timescales from seasons to decades and with large secular trends. The waveguides are dependent on meridional potential temperature gradients generated by land and sea surface temperatures (and topography), which are in turn modified by systematic trends in radiative forcings such as due to anthropogenic climate change. That secular trends in nonlinear systems can be characterised as regime transitions, often in response to systematic changes in external forcing, has been well established for example by Lorenz (2006). This implies that we can expect climatic variability and change to manifest in part through changes in the residence behaviour of the waveguide modes described here.

Acknowledgments The authors would like to thank an anonymous referee and in particular Rupert Klein (FU Berlin, Germany) for many insightful comments that greatly added to the clarity and readability of this paper. T.J.O. acknowledges funding support by an Australian Research Council Future Fellow (Grant FT120100008) and the Australian Climate Change Science Program. C.F. was supported by the German Research Foundation (DFG) through the cluster of excellence CliSAP. I.H. has been partially funded by the Mercator Fellowship of Deutsche Forschungsgemeinschaft (DFG) through Grant CRC 1114.

References

- Akaike H (1974) A new look at the statistical model identification. *IEEE Trans Autom Control* 19(6):716–723
- Akaike H (1988) Information theory and an extension of the maximum likelihood principle. In: Parzen E, Tanabe K, Kitagawa G (eds) *Selected papers of Hirotugu Akaike*. Springer, New York
- Ambrizzi T, Hoskins BJ, Hsu H-H (1995) Rossby wave propagation and teleconnection patterns in the austral winter. *J Atmos Sci* 52(21):3661–3672
- Ambrizzi T, Hoskins BJ (1997) Stationary Rossby wave propagation in a baroclinic atmosphere. *Q J R Meteorol Soc* 123:919–928
- Barnes EA, Slingo J, Woollins T (2012) A methodology for the comparison of blocking climatologies across indices, models and climate scenarios. *Clim Dyn* 38:2467–2481
- Barnston AG, Livezey RE (1987) Classification, seasonality and persistence of low-frequency atmospheric circulation patterns. *Mon Weather Rev* 115(6):1083–1126
- Branstator G (1983) Horizontal energy propagation in a barotropic atmosphere with meridional and zonal structure. *J Atmos Sci* 40:1689–1708
- Branstator G (2002) Circumglobal teleconnections, the jet stream waveguide, and the North Atlantic Oscillation. *J Clim* 15(14):1893–1910
- Bowler N, Arribas A, Mylne K, Robertson K, Beare S (2009) The MOGREPS short range ensemble prediction system. *Q J R Meteorol Soc* 134:703–722
- Burnham KP, Anderson DR (2002) *Model selection and multimodel inference: a practical information-theoretic approach*, 2nd edn. Springer. ISBN:0-387-95364-7
- Charney J (1947) The dynamics of long waves in a baroclinic westerly current. *J Meteorol* 4:132–162

- Charney J, DeVore J (1979) Multiple flow equilibria in the atmosphere and blocking. *J Atmos Sci* 36:1205–1216
- Chen T-C, Chen J-M (1997) On the relationship between the streamfunction and velocity potential of the Madden–Julian oscillation. *J Atmos Sci* 54:679–685
- Colucci SJ (1985) Explosive cyclogenesis and large scale circulation changes: implications for the onset of blocking. *J Atmos Sci* 42:2701–2719
- Colucci SJ (1987) Comparative diagnosis of blocking versus non-blocking planetary-scale circulation changes during synoptic-scale cyclogenesis. *J Atmos Sci* 44:124–139
- de Wiljes J, Putzig L, Horenko I (2014) Discrete non homogeneous and non stationary logistic and Markov regression models for spatiotemporal data with unresolved external influences sets. *Commun Appl Math Comput Sci* 9:1–46
- Ding Q, Steig EJ, Battisti DS, Wallace JM (2012) Influence of the tropics on the southern annular mode. *J Clim* 25:6330–6348
- Dole RM (1986) Life cycles of persistent anomalies and blocking over the North Pacific. *Adv Geophys* 29:31–69
- Dole RM, Gordon ND (1983) Persistent anomalies of the extra-tropical Northern Hemisphere wintertime circulation: geographical distribution and regional persistence characteristics. *Mon Weather Rev* 111:1567–1586
- Eady E (1949) Long waves and cyclone waves. *Tellus* 1:33–52
- Franzke CLE, O’Kane TJ, Monselesan DP, Risbey JS, Horenko I (2015) Systematic attribution of observed Southern Hemispheric circulation trends to external forcing and internal variability. *Nonlinear Process Geophys Discuss* 2:675–707
- Frederiksen JS (1982) A unified three dimensional instability theory for the onset of blocking and cyclogenesis. *J Atmos Sci* 39:969–982
- Frederiksen JS (1983) A unified three dimensional instability theory for the onset of blocking and cyclogenesis. Part II. *J Atmos Sci* 40:2593–2609
- Frederiksen CS, Frederiksen JS, Sisson JM, Osbrough SL (2011) Changes and projections in Australian winter rainfall and circulation: anthropogenic forcing and internal variability. *Int J Clim Change Impacts Responses* 2(3). ISSN:1835–7156
- Frederiksen JS, Lin H (2013) Tropical–extratropical interactions of intraseasonal oscillations. *J Atmos Sci* 70:3180–3197
- Frederiksen JS, Webster PJ (1988) Alternate theories of atmospheric teleconnections and low-frequency fluctuations. *Rev Geophys* 26(3):459–494
- Freitas ACV, Ambrizzi T (2012) Changes in the austral winter Hadley circulation and the impact on stationary Rossby wave propagation. *Adv Meteorol* 980816:1–15
- Freitas ACV, Frederiksen JS, Whelan J, O’Kane TJ, Ambrizzi T (2015) Observed and simulated inter-decadal changes in the structure of Southern Hemisphere large-scale circulation. *Clim Dyn* 25 pp. doi:10.1007/s00382-015-2519-z
- Gerber S, Horenko I (2014) On inference of causality for discrete state models in a multiscale context. *Proc Natl Acad Sci USA*. doi:10.1073/pnas.1410404111
- Granger CWJ (1988) Some recent development in a concept of causality. *Econometrics* 39:199–211
- Hannachi A, Jolliffe IT, Stephenson DB (2007) Empirical orthogonal functions and related techniques in atmospheric science: a review. *Int J Climatol* 27:1119–1152
- Horenko I (2009) On robust estimation of low-frequency variability trends in discrete Markovian sequences of atmospheric circulation patterns. *J Atmos Sci* 66:2059–2072
- Horenko I (2010) On clustering of non-stationary meteorological time series. *Dyn Atmos Oceans* 49:164–187
- Horenko I (2010) On the identification of nonstationary factor models and their application to atmospheric data analysis. *J Atmos Sci* 67(5):1559–1574
- Horenko I (2010) Finite element approach to clustering of multidimensional time series. *SIAM J Sci Comput* 31(1):62–83
- Horenko I (2011) On the analysis of nonstationary categorical data time series: dynamical dimension reduction, model selection, and applications to computational sociology. *Multiscale Model Simul* 9(4):1700–1726
- Hoskins BJ (1991) Towards a PV- θ view of the general circulation. *Tellus* 43A:27–35
- Hoskins BJ (2015) Potential vorticity and the PV perspective. *Adv Atmos Sci* 32:2–9
- Hoskins BJ, Karoly DJ (1981) The steady linear responses of a spherical atmosphere to thermal and orographic forcing. *J Atmos Sci* 38:1179–1196
- Hoskins BJ, Ambrizzi T (1993) Rossby wave propagation on a realistic longitudinally varying flow. *J Atmos Sci* 50:1661–1671
- Karoly DJ (1983) Rossby wave propagation in a barotropic atmosphere. *Dyn Atmos Oceans* 7:111–125
- Karoly DJ, Plumb RA, Ting M (1989) Examples of the horizontal propagation of quasi-stationary waves. *J Atmos Sci* 46:2802–2811
- Kobayashi S, Ota Y, Harada Y, Ebata A, Moriya M, Onoda H, Onogi K, Kamahori H, Kobayashi C, Endo H, Miyaoka K, Takahashi K (2015) The JRA-55 reanalysis: general specifications and basic characteristics. *J Meteor Soc Jpn* 93(1):5–48
- Legras B, Ghil M (1985) Persistent anomalies, blocking and variations in atmospheric predictability. *J Atmos Sci* 42(5):432–471
- Liniger MA, Davies HC (2004) Seasonal differences in extratropical potential vorticity variability at tropopause levels. *J Geophys Res* 109:D17102
- Li X, Gerber EP, Holland DM, Yoo C (2015) A Rossby wave bridge from the tropical Atlantic to West Antarctica. *J Clim* 28:2256–2273
- Lorenz EN (1956) Empirical orthogonal functions and statistical weather prediction. Technical report, Statistical Forecast Project Report 1, Dep of Meteor, MIT, 49 pp
- Lorenz EN (2006) Regimes in simple systems. *J Atmos Sci* 63:2056–2073
- Luo D, Cha J, Zhong L, Dai A (2014) A nonlinear multiscale interaction model for atmospheric blocking: the eddy-blocking matching mechanism. *Q J R Meteorol Soc*. doi:10.1002/qj.2337
- Lynch P (1988) Deducing the wind from vorticity and divergence. *Mon Weather Rev* 116:86–93
- Metzner P, Putzig L, Horenko I (2012) Analysis of persistent nonstationary time series and applications. *Commun Appl Math Comput Sci* 7(2):175–229
- Mo KC, Higgins RW (1998) The Pacific–South American modes and tropical convection during the Southern Hemisphere winter. *J Atmos Sci* 126:1581–1596
- Mo KC, Paegle JN (2001) The Pacific–South American modes and their downstream effects. *Int J Climatol* 21:1211–1229
- Molteni F, Buizza R, Palmer T, Petroliagis T (1996) The ECMWF ensemble prediction system: methodology and validation. *Q J R Meteorol Soc* 122:73–119
- O’Kane TJ, Frederiksen JS (2008) A comparison of statistical dynamical and ensemble prediction methods during blocking. *J Atmos Sci* 65:426–447
- O’Kane TJ, Naughton MJ, Xiao Y (2008) The Australian community climate and earth system simulator global and regional ensemble prediction system. *ANZIAM J* 50:C385–C398
- O’Kane T, Risbey J, Franzke CLE, Horenko I, Monselesan D (2013) Changes in the meta-stability of the mid-latitude Southern Hemisphere circulation and the utility of nonstationary cluster analysis and split flow blocking indices as diagnostic tools. *J Atmos Sci* 70(3):824–842
- Pazo D, Rodriguez M, Lopez J (2010) Spatio-temporal evolution of perturbations in ensembles initialized by bred, Lyapunov and singular vectors. *Tellus* 62A:10–23

- Pezza AB, van Rensch P, Cai W (2012) Severe heat waves in Southern Australia: synoptic climatology and large scale connections. *Clim Dyn* 38:209–224
- Phillips NA (1954) Energy transformations and meridional circulations associated with simple baroclinic waves in a two-level, quasi-geostrophic model. *Tellus* 6(x):273–286
- Plumb RA (1985) On the three-dimensional propagation of stationary waves. *J Atmos Sci* 42:217–229
- Plumb RA (1986) Three-dimensional propagation of transient quasi-geostrophic eddies and its relationship with the eddy forcing of the time-mean flow. *J Atmos Sci* 43:1657–1678
- Qin J, Robinson WA (1993) On the Rossby wave source and the steady linear response to tropical forcing. *J Atmos Sci* 50(12):1819–1823
- Rogers JC, van Loon H (1982) Spatial variability of sea level pressure and height anomalies over the Southern Hemisphere. *Mon Weather Rev* 110:1375–1392
- Risbey JS, O’Kane TJ, Monselesan DP, Franzke CLE, Horenko I (2015) Metastability of Northern Hemisphere teleconnection modes. *J Atmos Sci* 72(1):35–54
- Sardeshmukh PD, Hoskins BJ (1988) The generation of global rotational flow by steady idealized tropical divergence. *J Atmos Sci* 45(7):1228–1251
- Shimizu MH, de Albuquerque Cavalcanti IF (2011) Variability patterns of Rossby wave source. *Clim Dyn* 37:441–454
- Takaya K, Nakamura I (2001) A formulation of a phase-independent wave-activity flux for stationary and migratory quasi-geostrophic eddies on a zonally varying basic flow. *J Atmos Sci* 58:608–627
- Tibaldi S, Tosi E, Navarra A, Pedulli L (1994) Northern and Southern Hemisphere seasonal variability of blocking frequency and predictability. *Mon Weather Rev* 122:1971–2003
- Toth Z, Kalnay E (1997) Ensemble forecasting at NCEP and the breeding method. *Mon Weather Rev* 125:3297–3319
- Vallis G (2010) *Atmospheric and oceanic fluid dynamics*. Cambridge University Press, Cambridge
- Vercauteren N, Klein R (2014) A clustering method to characterize intermittent bursts of turbulence and interaction with submesoscale motions in the stable boundary layer. *J Atmos Sci* 72:1504–1517
- Zidikheri M, Frederiksen JS, O’Kane TJ (2007) Multiple equilibria and atmospheric blocking. In: Denier J, Frederiksen JS (eds) *Frontiers in turbulence and coherent structures*, chap 4, pp 59–86. World Scientific Pub. Co. Inc., Singapore